

Electronic Supporting Material for

Functional mapping reveals mechanistic clusters for OER catalysis across (Cu-Mn-Ta-co-Sn-Fe)O_x composition and pH space.

Helge S. Stein¹, Dan Guevarra¹, Aniketa Shinde¹, Ryan J. R. Jones¹, John M. Gregoire^{1}, Joel A. Haber¹*

Table of Contents

1. Experimental Details	Page S3
2. Composition measurement by XRF	Page S5
3. Confirmation of OER activity of Co-rich compositions at pH 3	Page S7
4. Scale-up and testing of lead compositions	Page S8
5. Visualization of electrochemical data.	
a. Figure S6. cMDS plots for the LaCeMnCoNiFeO _x	Page S9
b. Figure S7. cMDS plots for the CuMnTaCoNiFeO _x	Page S10
c. Figure S8. Pseudoternary maps for (Cu-Mn-Ta-Co-Sn-Fe)O _x	Pages S12-S26
d. Figure S9. Pseudoternary maps for (Ni-Fe-La-Ce-Co-Mn)O _x	Pages S27-S41
e. Figure S10. Pseudoternary maps for (Ni-Fe-Cu-Mn-Co-Ta)O _x	Pages S42-S56

Experimental Details

Ink Preparation. Metal oxide precursor inks were prepared to be chemically and rheologically compatible with Epson 4880 InkJet printer technology. An ink-base stock solution was prepared by mixing together in 500 mL of 200 Proof Ethanol (Koptec) 13.0 g of Pluronic F127 (x), 16.0 mL of glacial acetic acid (T.J. Baker), 6.0 mL of concentrated nitric acid (EMD) and stirring for at least 12 hours to produce a clear colorless solution. 20.0 mL of this stock solution was added to 3.3 mmoles of each metal precursor ($\text{Cu}(\text{NO}_3)_2 \cdot 3\text{H}_2\text{O}$ (0.815 g, 99-104%, Sigma Aldrich), 0.940 g $\text{Mn}(\text{NO}_3)_2 \cdot 4\text{H}_2\text{O}$ (0.940 g, 99.8%, Alfa Aesar), TaCl_5 (1.29 g, 99.99%, Sigma Aldrich), $\text{Co}(\text{NO}_3)_2 \cdot 6\text{H}_2\text{O}$ (0.99 g, 98%, Sigma Aldrich), $\text{SnCl}_2 \cdot 2\text{H}_2\text{O}$ (0.194, 98%, Sigma Aldrich), $\text{Fe}(\text{NO}_3)_3 \cdot 9\text{H}_2\text{O}$ (1.50 g, 99.95%, Sigma Aldrich), $\text{La}(\text{NO}_3)_3 \cdot 6\text{H}_2\text{O}$ (1.42 g, 99.99%, Sigma Aldrich), $\text{Ce}(\text{NO}_3)_3 \cdot 6\text{H}_2\text{O}$ (1.53, 99.99%, Sigma Aldrich), $\text{Ni}(\text{NO}_3)_2 \cdot 6\text{H}_2\text{O}$ (0.977 g, 98.5%, Sigma Aldrich)) and stirred for 30 minutes to produce clear solutions. The TaCl_5 ink was additionally filtered through 0.45 μm PTFE Acrodisc syringe filters before use.

Printing. Each ink was loaded into a specific channel of a modified Epson Stylus Pro 4880, 8 channel inkjet printer (C2Fast, Hangzhou Nanov, Hangzhou 310000, China). The 2121 discrete composition samples spanning the 15 pseudo-quaternary spaces in 10 at% composition steps were deposited onto 100 x 150 x 1.0 mm fluorine-doped tin oxide (FTO, Tech 7) coated soda lime glass. The composition of each 1 mm x 1 mm sample was controlled by the amount of each ink delivered, as specified by printing color TIFF images of the library map with each sample a unique mixture of up to 4 colors (4 metal oxide precursor inks). The ink was delivered by nearly simultaneously delivery from all the ink channels, enabling thorough mixing of the liquid inks on the substrate.

Thermal Processing and Calcination. Immediately after printing, the plates were placed in a 37 °C oven, at which temperature the Pluronic F127 gels and inhibits formation of coffee rings and segregation of metals during drying. After 12-16 h of pre-drying the plates are transferred to a 67 °C oven for an additional 20-24 h to complete solvent evaporation and initial condensation of the oxide precursors. The plates were then calcined to form the metal oxides and remove carbon containing ink components by processing in a tube furnace in 0.395 atm O_2 at 400 °C for 10 h.

Parallel Electrochemical Treatment System (PETS). To provide initial electrochemical conditioning, and avoid measurement of initial electrochemical corrosion, each plate was electrochemically treated in the electrolyte solution for 2 h under controlled, low current conditions. The treatment system and methods are described in the main paper, in a dedicated instrument paper illuminating the need to limit current density during electrochemical treatment under potentially corroding conditions to maintain uniformity across the plate¹, and in further detail (included exploded schematics of the system) in a paper on discovery of OER catalysts under acidic conditions². After the PETS treatment the plate was immediately rinsed with the same electrolyte solution used for the electrochemical treatment, but which did not contain the Na_2SO_4 supporting electrolyte, and then the liquid was blown from the surface using a stream of compressed air. The electrolyte solutions used for PETS and subsequent SDC have measured conductivities of 38.0, 43.0, 38.2, and 52.9 millSiemens for pH 3, 7, 9, 13, respectively. In comparison, the electrolyte used in work characterizing the electrochemical performance of the SDC is 1.0 M NaOH which has a conductivity of 179.6 mS.³

Scanning Drop Electrochemical cell measurement. Serial electrochemical measurements were made on each sample as described in the paper. The SDC has been described in detail previously, and is shown schematically in **Figure S1**. In brief, a sample specific electrical contact is made sequentially to each 1mm x 1mm sample deposited on the common working electrode composed of FTO on glass using a droplet of the electrolyte. The electrolyte is delivered by gravity feed through a capillary tube in contact with a Pt counter electrode, and flows continuously during operation at a rate sufficient to replenish the drop volume over 10 times per second. The electrolyte is syphoned away by the three amber tubes in the schematic to maintain the droplet over a single sample. A micro reference electrode is inserted into the droplet between the capillary delivery tube and the working electrode. Due to the very small dimensions of the droplet and distance between the reference and working electrode solution resistance is minimal and no IR compensation is employed in these measurements. After completion of the sequence of electrochemical measurements on one sample the substrate is rastered to position the SDC cell and droplet over the next sample, with a one second delay between translation and initiation of electrochemical measurements to allow for drop stabilization. The sequential measurement of the 2121 samples on each plate requires approximately 20 h to complete, during which time any electrolyte left behind the translating droplet does dry. This dried electrolyte was removed by rinsing the plate with the same pH buffer solution but which did not contain the Na_2SO_4 supporting electrolyte, and then the liquid blown from the surface with a stream of compressed air.

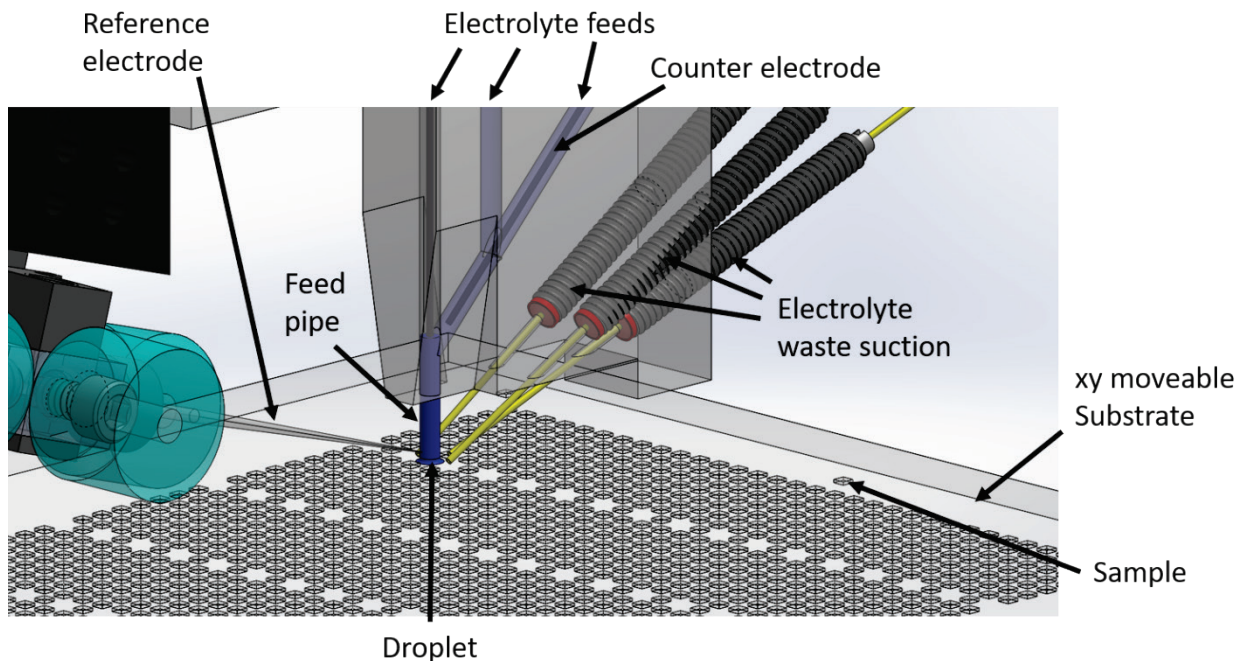


Figure S1 Schematic drawing of the SDC setup used in this study. The scanning droplet cell assembly consists

Composition measurement by XRF. The composition of a subset of 156 samples was measured by XRF and calibration standards used to convert cps of characteristic X-ray peaks to nmoles per cm² of each metal for each sample. The selected samples systematically span the compositions within each of the 15 pseudoquaternary spaces as shown in **Figure S2a**. In addition to each single metal oxide, 2, 3, and 4 metal oxide mixtures were also measured with addition of 20 at% of the 2nd, 3rd, and 4th metals (eg. A₁₀₀, A₈₀B₂₀, A₈₀C₂₀, A₈₀D₂₀, A₆₀B₂₀C₂₀, A₆₀B₂₀D₂₀, A₆₀C₂₀D₂₀, A₄₀B₂₀C₂₀D₂₀). A single plate was measured in the as-calcined state, prior to any electrochemistry, and a single plate was measured after electrochemistry (PETS plus SDC) in each of the four pH conditions. The distribution of each metal loading after electrochemistry at each pH relative to that of the control plate is presented in **Figure S2b**. The results for Sn are not presented, because the large background Sn signal from the substrate FTO prevents a meaningful measure of Sn loading. As is evident from this plot most materials are relatively stable in pH 13 and unstable in pH 3. Of the transition element metals, Ta is the most stable element across all pHs. The vertical distribution is indicative of statistical counting errors from Ta's relatively weak XRF signal. Co exhibits the most obvious trend in stability improvement with increasing pH, most samples are stable pH 9 and 13, but significant corrosion occurs at pH 3 and 7. It is interesting to note that the instability for Cu and Mn is virtually the same in pH 3 and 7. For Mn, little corrosion occurs at pH 9 and 13, but many samples show significant corrosion at pH 3 and 7. Interestingly, Cu is most stable at pH 9, and shows significant corrosion at both lower and higher pHs. Some slight improvements in stability resulting from co-addition of a particular 2nd metal are suggested by this plot. For instance, a stability increase of Fe in pH 9 through addition of Cu, or the increased stability of Cu, Mn, and Co with addition of Ta in pH 13.

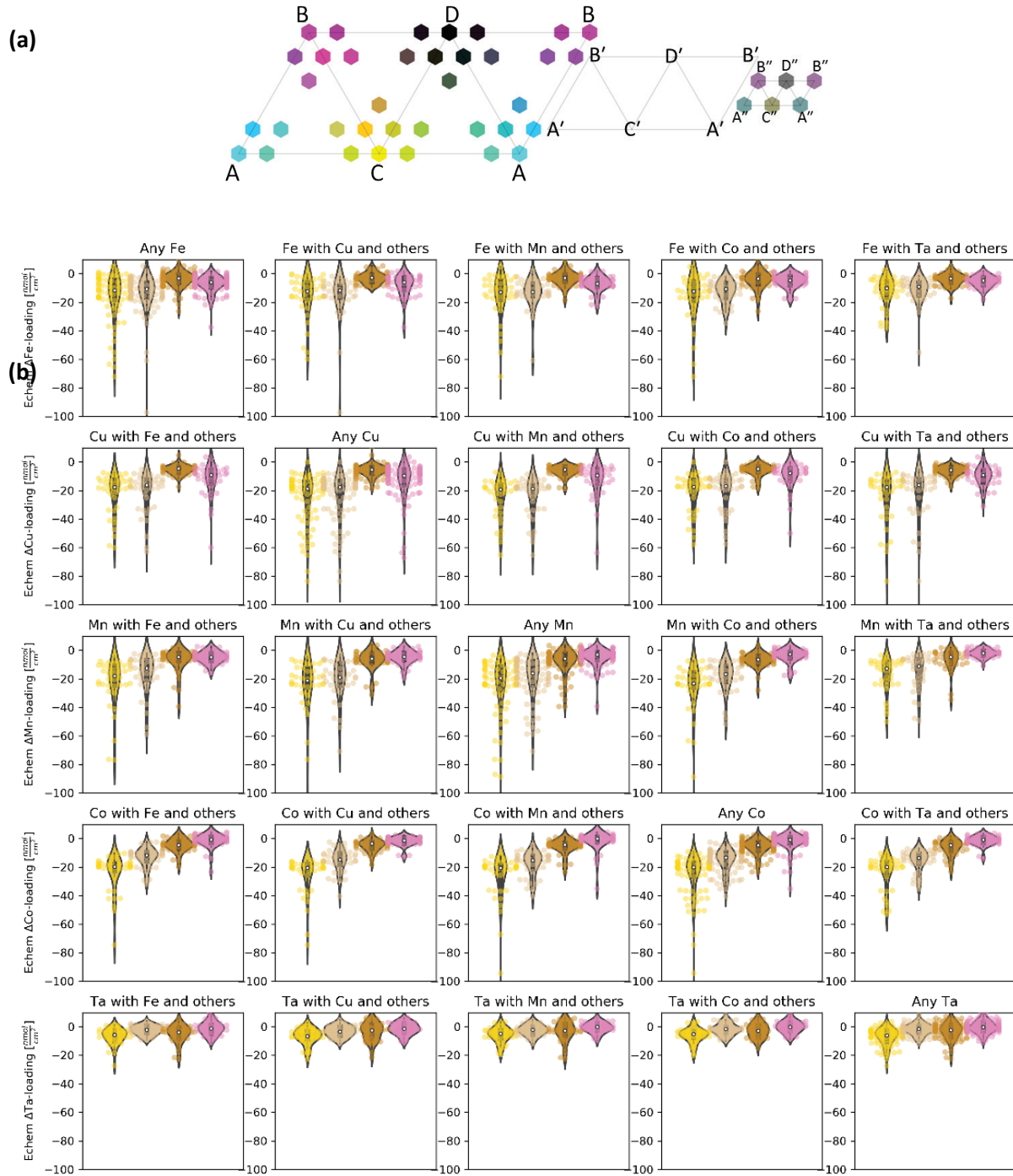


Figure S2 (a) The intended initial sample compositions measure by XRF for each pseudoquaternary composition space as an unwrapped tetrahedral representation of a psuedoquaternary composition space with 10 at% steps. A, B, C, and D are single metal oxide compositions; A', B', C', and D' are the apices of the middle shell of the tetrahedron were $A'=A_{70}B_{10}C_{10}D_{10}O_x$, etc.; and A'', B'', C'', and D'' are the apices of the core, where $A'' = A_{40}B_{20}C_{20}D_{20}O_x$, etc. (b) Violin plots of elemental loss (in nmoles/cm²) of each metal after electrochemistry relative to a calcined-only control plate as a function of pH. Elemental loss is shown as loading loss from before to after electrochemical treatment. This plot spans all

composition spaces in 20 at.% steps. Only samples containing an intended composition of >0 at.% of a particular element are included in each plot (ie. Only samples prepared to contain Fe are included in the top row of plots). Each panel shows the absolute loss of a particular metal with separate histogram and violin plot after electrochemical measurement at each pH (from left to right 3 (yellow), 7 (beige), 9 (brown), and 13 (pink)). The diagonal of panels from top-left to bottom-right shows the loss of each metal from any sample containing that metal. The other panels in that row show the loss of that metal from all samples that also contain a specified 2nd metal (and possible a 3rd and 4th metal). Comparison of these panels with a specified 2nd metal to the other panels suggests if a particular 2nd metal may stabilize (or destabilize) the primary metal to corrosion at different pHs.

Confirmation of OER activity of Co-rich compositions at pH 3. As shown in Figure 5a) at pH 3 Cu₁₀Mn₁₀Co₈₀O_x is identified as the most active initially deposited composition, with several nearby Co-rich compositions containing Mn or Cu in the top 7 highest performing compositions. To validate this discovery and to more precisely identify the optimal composition(s), new pseudoquaternary composition libraries were prepared at 5at% for the composition space (Co-Cu-Mn-Sn)O_x. These libraries were calcined, electrochemically treated in the PETS system, and the performance measured using the SDC system at pH 3, as described above. The 20 pseudoternary slices containing constant concentrations of Sn are shown in **Figure S3**. In addition to confirming the high activity of Co-rich, Cu and Mn containing compositions in the largest pseudoternary slice containing 0 at% Sn, the previously unsynthesized compositions containing 5 at% Sn are observed to have similar or slightly higher activity, while the 10 at% Sn slice shows reduced activity, consistent with prior synthesis at 10 at% composition steps.

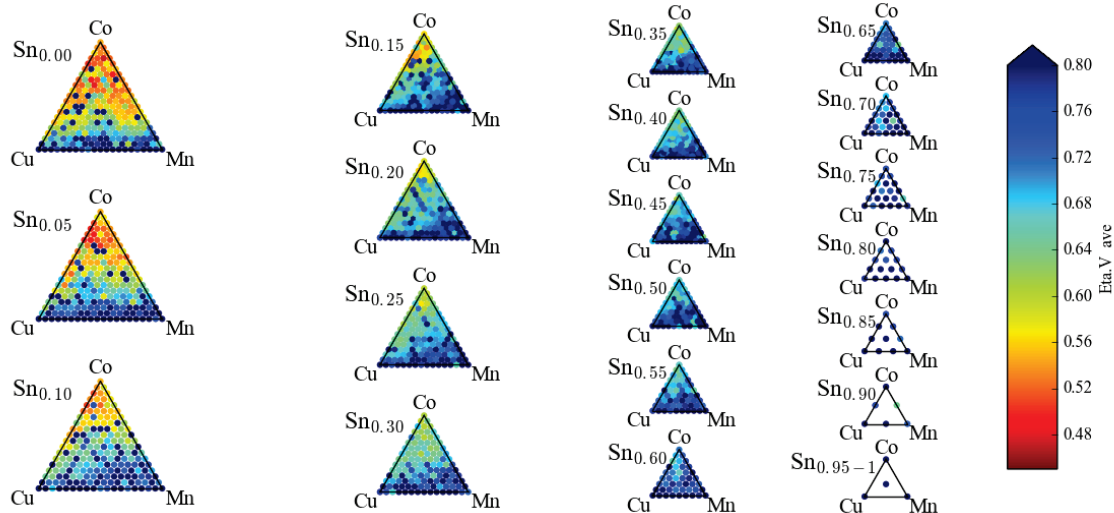


Figure S3. Constant Sn-loading pseudoternary composition maps at 5 at% composition of (Co-Cu-Mn-Sn)O_x OER overpotential from CP = 3 mA/cm².

Scale-up and testing of lead compositions. Based upon the optimal compositions identified in the original 10 at% composition step study and the 5 at% composition step follow-up synthesis, promising lead compositions were identified for further scale-up and testing. Figure S4 displays the 3 mA/cm² CP measurement performed on a glassy carbon rotating disc electrode onto which the $\text{Co}_{0.8}\text{Cu}_{0.1}\text{Mn}_{0.1}\text{O}_x$ composition was deposited by ink jet printing and calcination as described above for the composition libraries. The material was not PETS processed prior to this measurement. An average overpotential of 516 mV vs OER is needed to sustain 3mA/cm². After about 4100 s the required overpotential increases rapidly because catalyst corrosion nears completion or the catalyst detaches from the glassy carbon electrode. As catalyst detachment from the glassy carbon RDE was observed in some cases, catalysts were also tested by clamping a cell with an o-ring gasket to ~1 cm² films ink jet printed onto FTO coated glass plates, with electrolytes flowing continuously through the cell. Figure S5 shows the 2 hr 3 mA/cm² CP measurements for several compositions selected from the 5 at% composition library screening were prepared and tested in pH 3 electrolyte. The electrolyte additionally contained a total of 120 micromolar Co + Cu + Mn nitrate ions in proportion to their intended film concentrations.

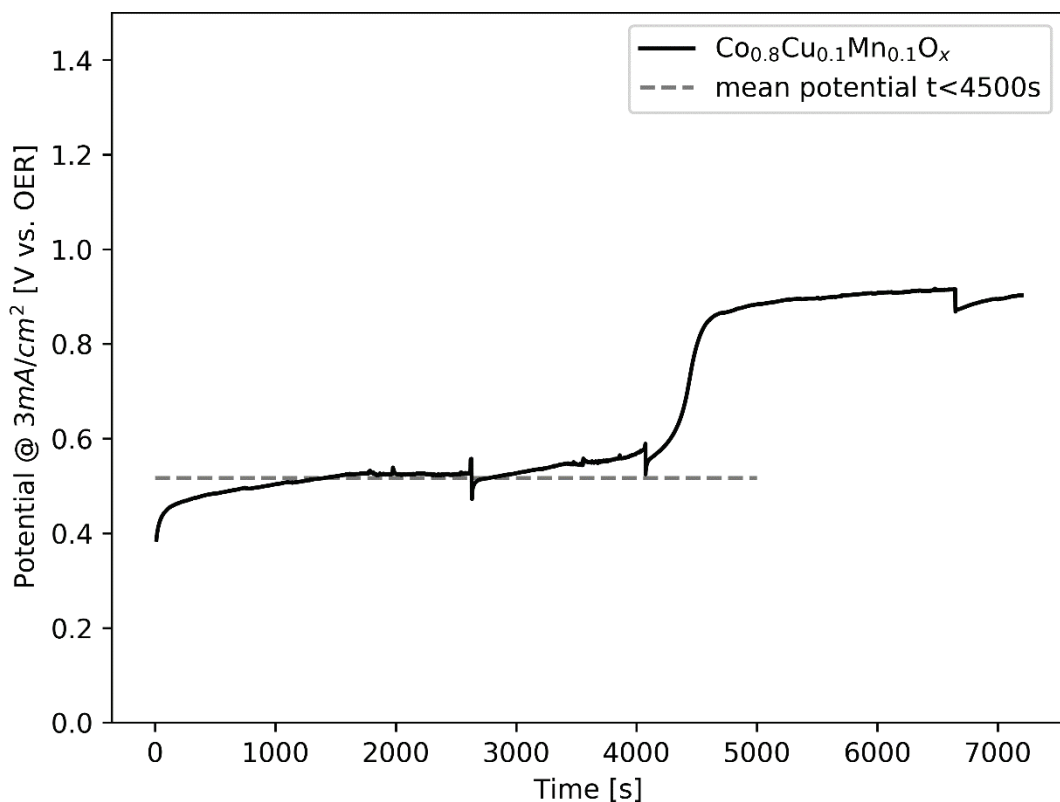


Figure S4 Rotating disc electrode (RDE) CP @ 3mA/cm² with a film of $\text{Co}_{0.8}\text{Cu}_{0.1}\text{Mn}_{0.1}\text{O}_x$ deposited by ink jet printing onto a glassy carbon disc, tested in pH 2.8 (10 mM H_3PO_4 /40 mM NaH_2PO_4 + 0.25 M Na_2SO_4) with dissolved $\text{Cu}(\text{NO}_3)_2$ (10 µM), $\text{Mn}(\text{NO}_3)_2$ (10 µM) and $\text{Co}(\text{NO}_3)_2$ (99 µM).

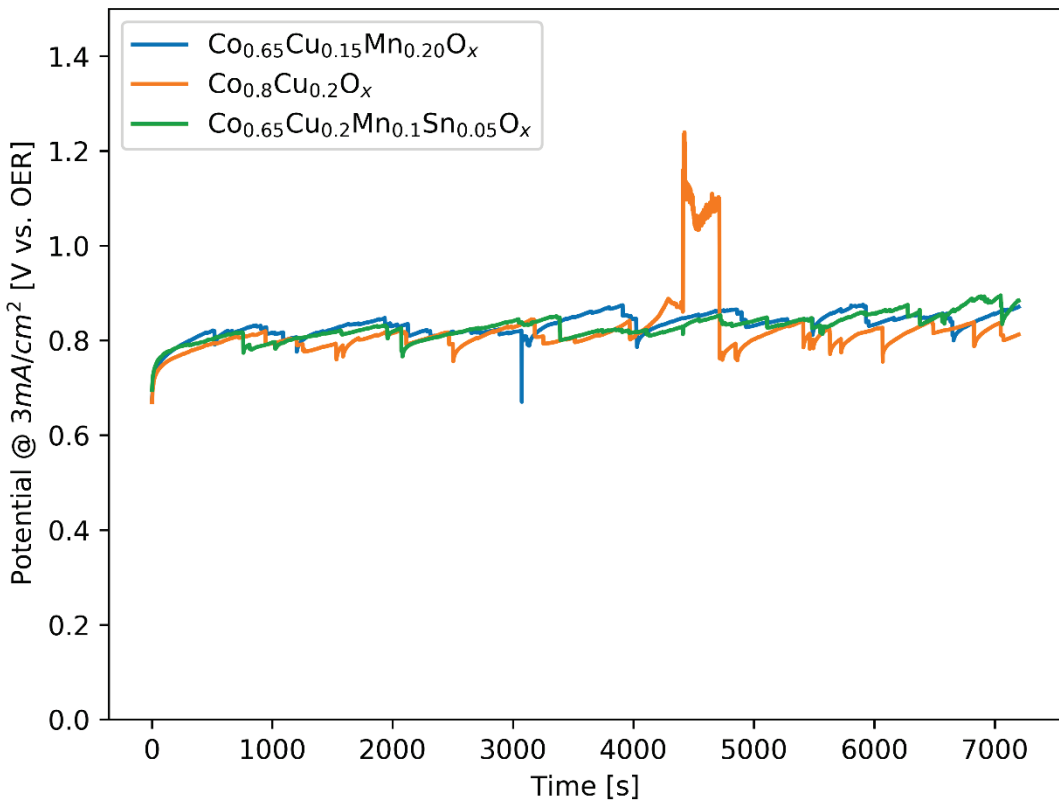


Figure S5 Selected compositions close to those discovered in Figure 5 tested in a recirculation cell for up to two hours. Most catalysts indicate good electrochemical stability but not quite the observed low overpotentials of the discovered system.

Visualization of electrochemical data. In order to visualize the OER catalytic performance in a manner comprehensible by a human being, the electrochemical data is reduced to a single scalar quantity for each composition, and then plotted as a function of initial intended composition. In this paper, only the average overpotential at 10 mA/cm² over the final seconds of the second CP measurement is used for each composition. Even with this significant reduction in data dimensionality, comprehending the OER behavior of 2121 compositions at 4 different pHs (8484 datapoints) is challenging. In previous publications we have represented the behavior as a color scale representing overpotential on pseudoquaternary composition plots in tetrahedrons, a series of pseudoternary slices through the tetrahedron, or as psedoternary slices unwrapping the tetrahedron, as shown in **Figure S2a**. In these prior publication we have usually reported the results from only one such pseudoquaternary composition space measured in a single electrolyte, occasionally with the same composition investigated at three catalyst loadings. In the experiment reported in this paper, there are 60 unique pseudoquaternary representations of the data. In addition, while we have reported only one 6 metal,

15 pseudoquaternary experiment in the main paper, additional 6 metal combinations have been investigated. This explosion of data requires a different visualization representation. Here we present two addition, Ni-containing composition spaces using the cMDS presentation unveiled in the main paper. $(La-Ce-Mn-Co-Ni-Fe)O_x$ is presented in **Figure S6** and $(Cu-Mn-Ta-Co-Ni-Fe)O_x$ is presented in **Figure S7**. To illustrate the relative complexity of comprehending the same data in the strictly more representative unwrapped tetrahedral representation, the $(Cu-Mn-Ta-Co-Sn-Fe)O_x$ results of the main paper are presented in **Figure S8**, those of the $(La-Ce-Mn-Co-Ni-Fe)O_x$ results in **Figure S9** and those of the $(Cu-Mn-Ta-Co-Ni-Fe)O_x$ results in **Figure S10**.

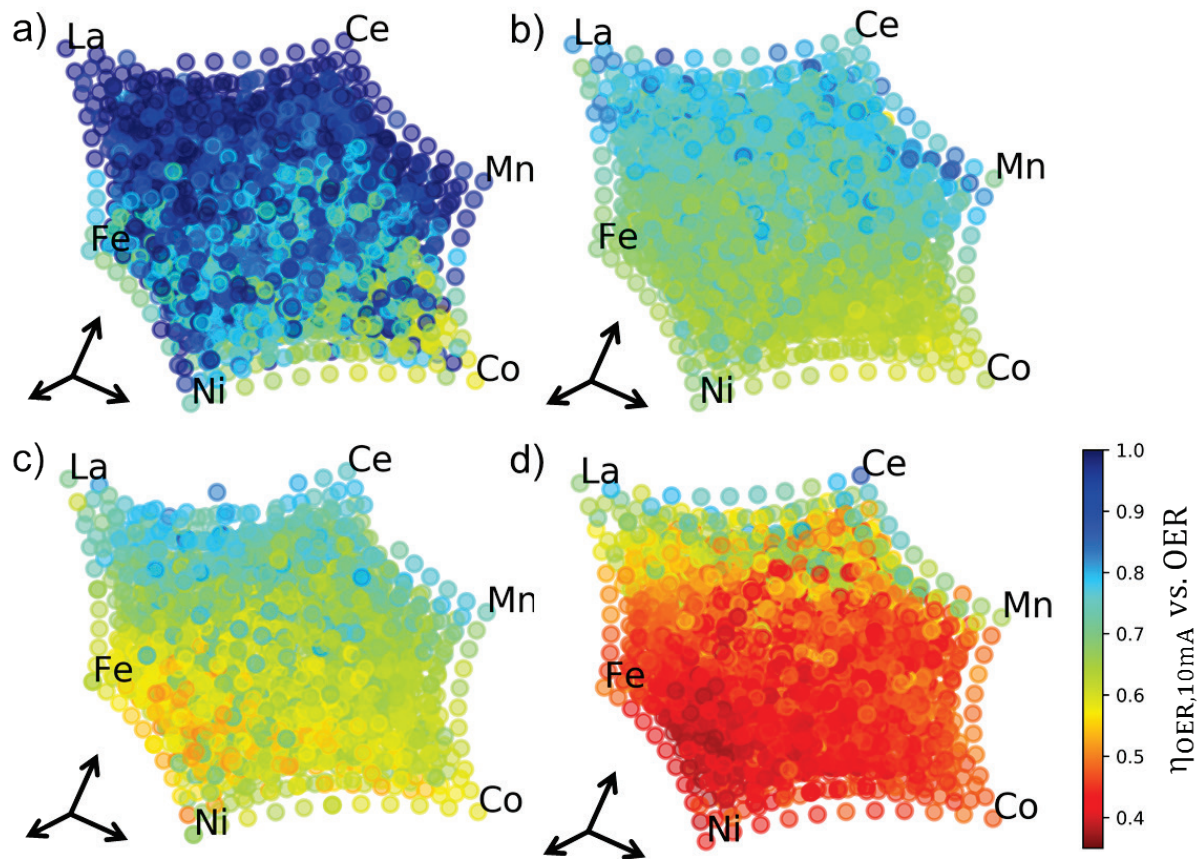


Figure S6. cMDS plots for the $LaCeMnCoNiFeO_x$ composition space $10\text{mA}/\text{cm}^2$ overpotential in (a) pH 3, (b) pH 7, (c) pH 9, and (d) pH 13

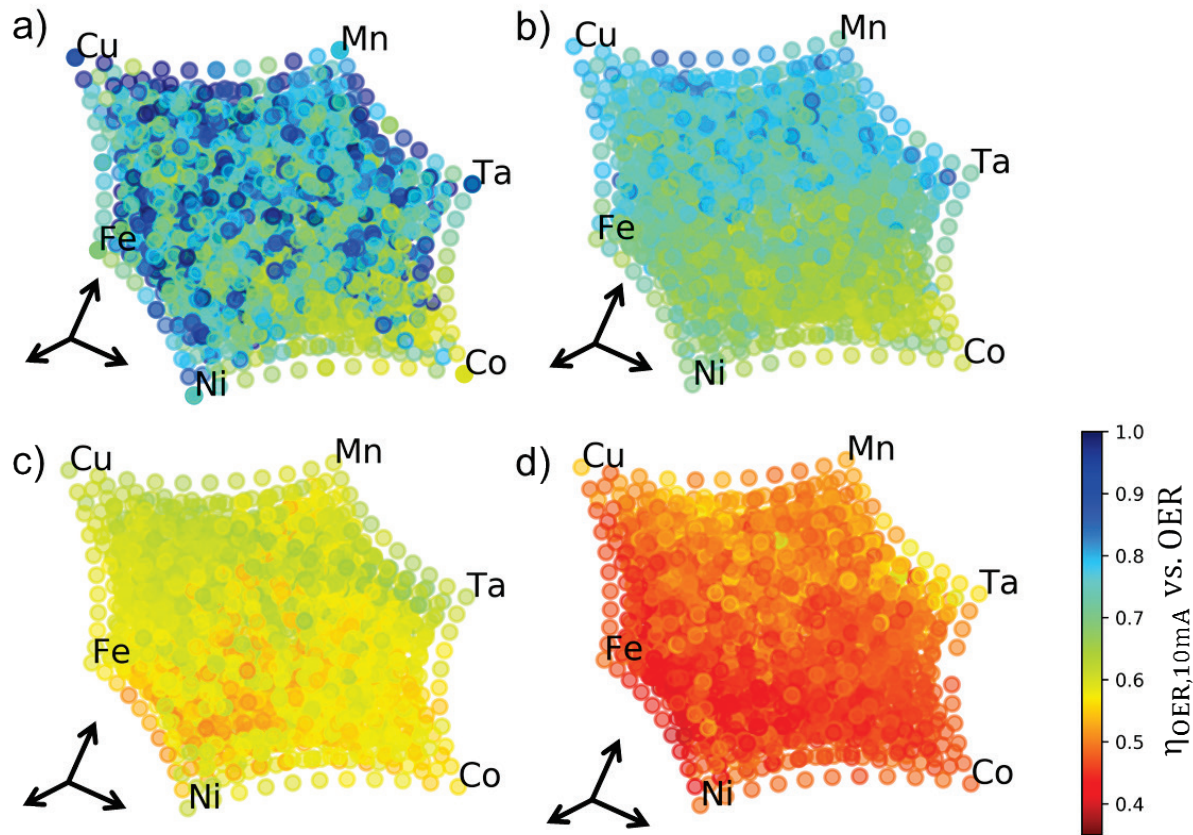
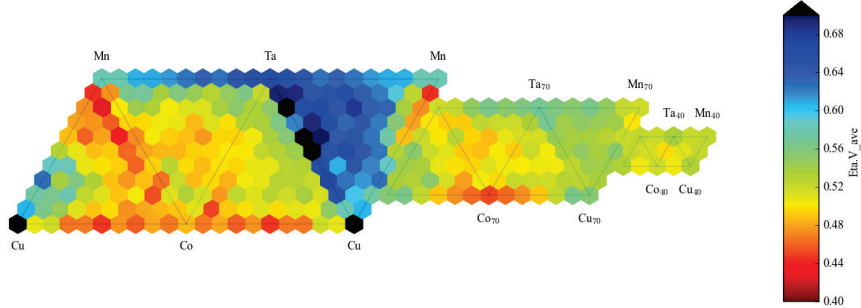
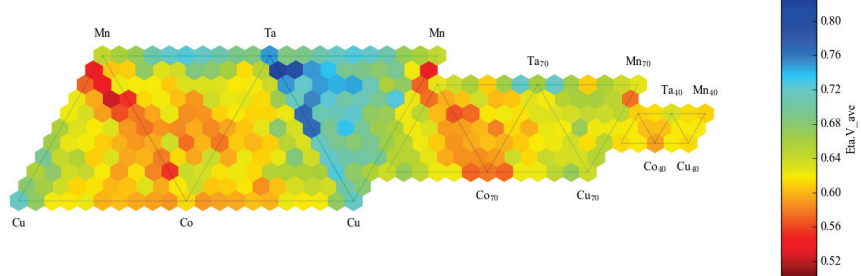


Figure S7. cMDS plots for the CuMnTaCoNiFeO_x composition space 10mA/cm² overpotential in (a) pH 3, (b) pH 7, (c) pH 9, and (d) pH 13

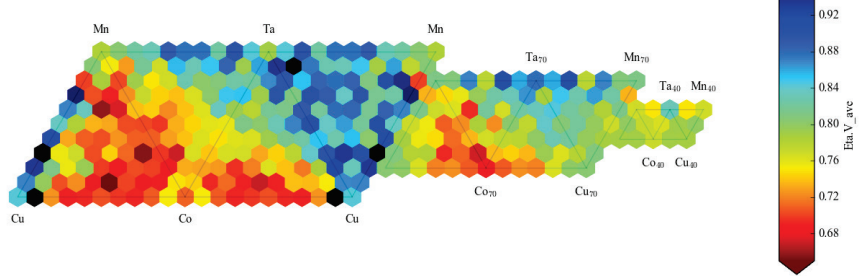
(a) pH 13



(b) pH 9



(c) pH 7



(d) pH 3

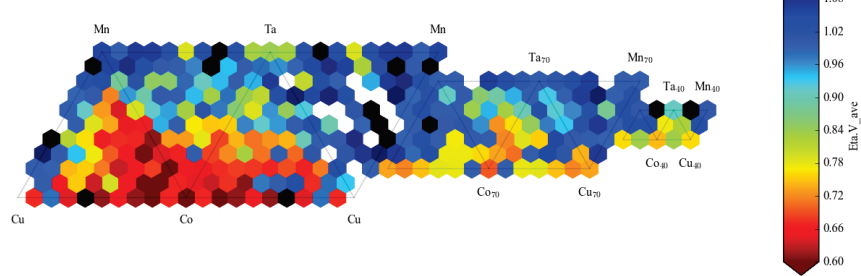
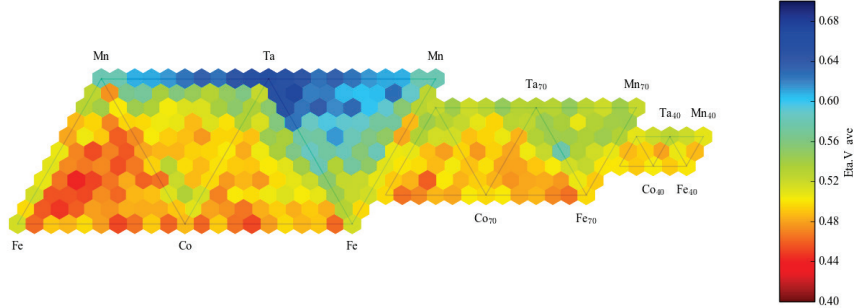
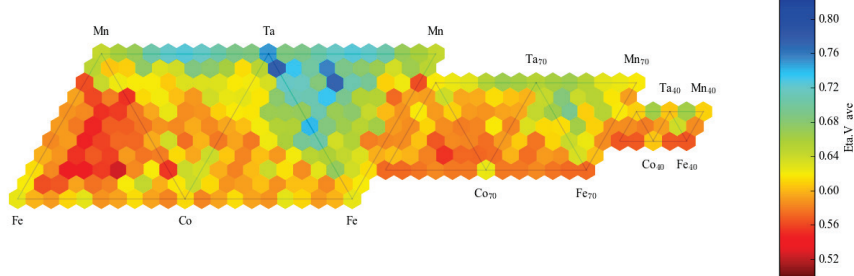


Figure S8-part 1. Composition map of η_{OER} at 10 mA cm^{-2} for the pseudoquaternary $(\text{Cu}-\text{Mn}-\text{Co}-\text{Ta})\text{O}_x$ in (a) pH 13, (b) pH 9, (c) pH 7, (d) pH 3 (note different color scale at each pH).

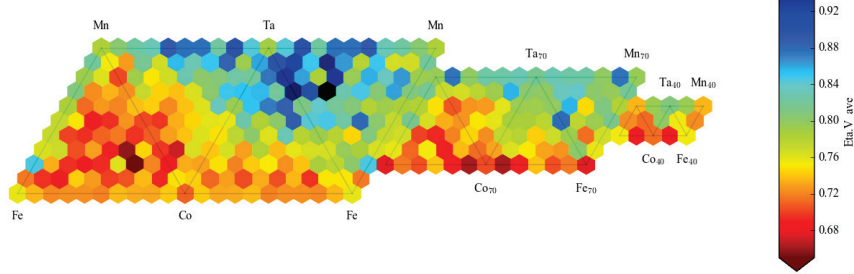
(a) pH 13



(b) pH 9



(c) pH 7



(d) pH 3

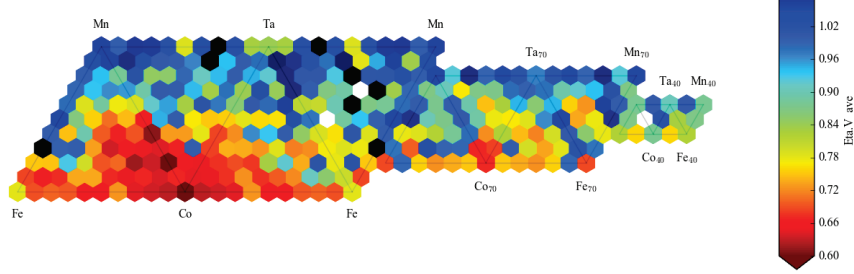
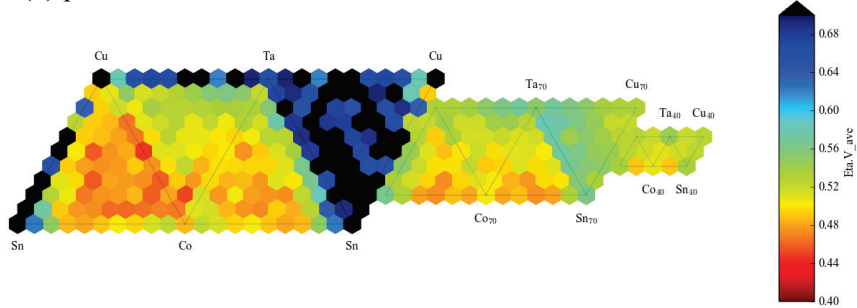
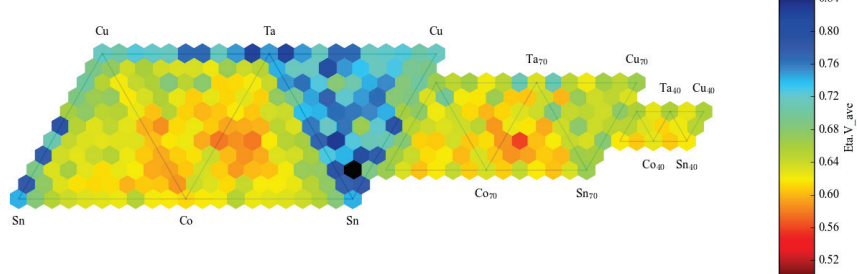


Figure S8-part 2. Composition map of η_{OER} at $10 \text{ mA}\cdot\text{cm}^{-2}$ for the pseudoquaternary $(\text{Fe}-\text{Mn}-\text{Co}-\text{Ta})\text{O}_x$ in (a) pH 13, (b) pH 9, (c) pH 7, (d) pH 3 (note different color scale at each pH).

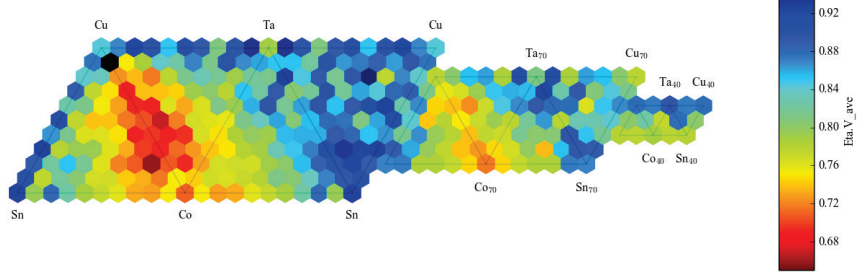
(a) pH 13



(b) pH 9



(c) pH 7



(d) pH 3

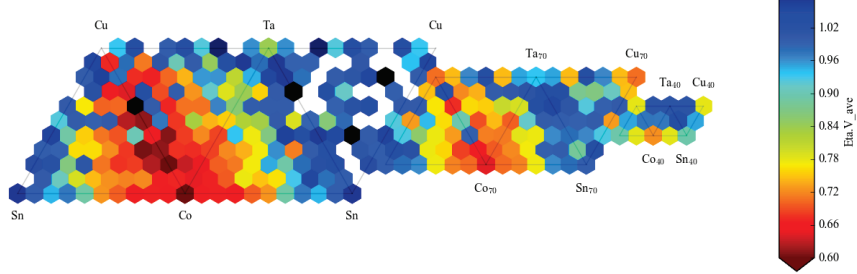
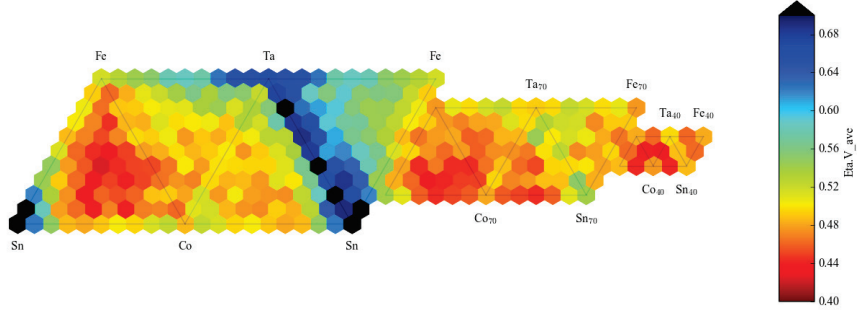
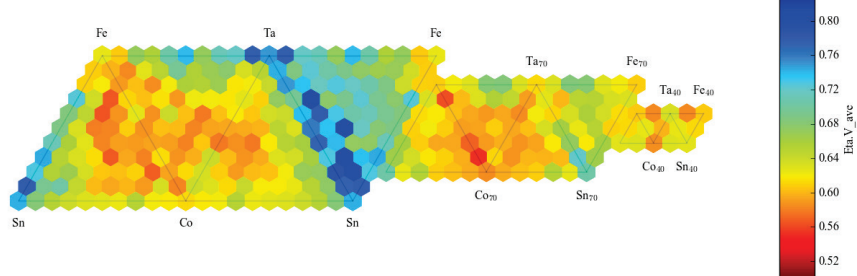


Figure S8-part 3. Composition map of η_{OER} at $10 \text{ mA}\cdot\text{cm}^{-2}$ for the pseudoquaternary $(\text{Sn}-\text{Cu}-\text{Co}-\text{Ta})\text{O}_x$ in (a) pH 13, (b) pH 9, (c) pH 7, (d) pH 3 (note different color scale at each pH).

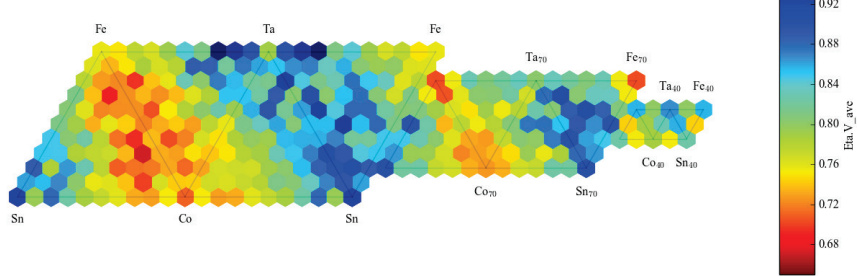
(a) pH 13



(b) pH 9



(c) pH 7



(d) pH 3

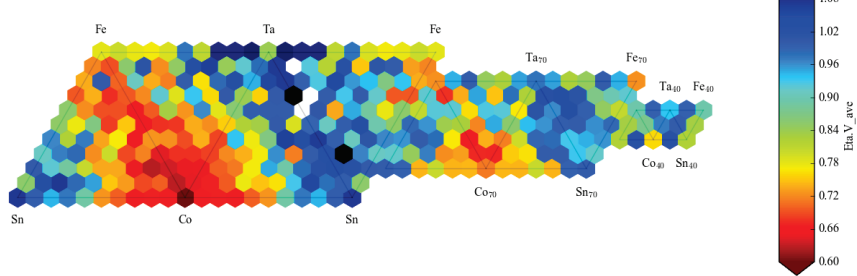
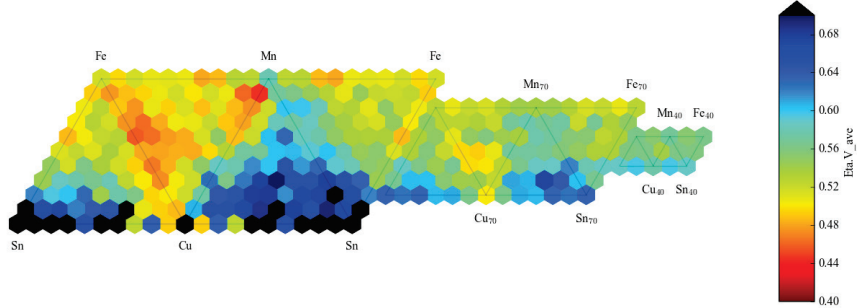
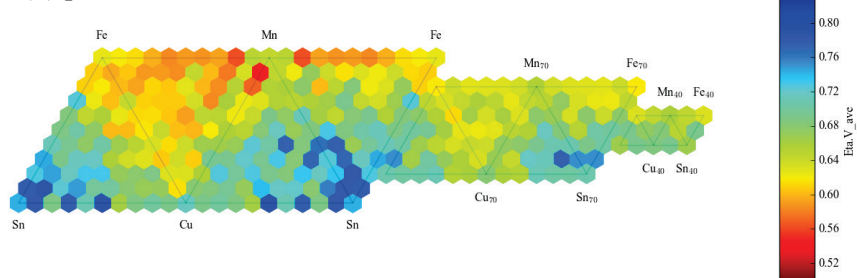


Figure S8-part 4. Composition map of η_{OER} at $10 \text{ mA}\cdot\text{cm}^{-2}$ for the pseudoquaternary $(\text{Sn}-\text{Fe}-\text{Co}-\text{Ta})\text{O}_x$ in (a) pH 13, (b) pH 9, (c) pH 7, (d) pH 3 (note different color scale at each pH).

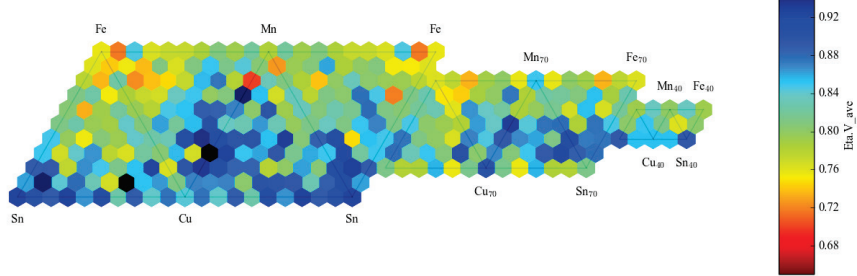
(a) pH 13



(b) pH 9



(c) pH 7



(d) pH 3

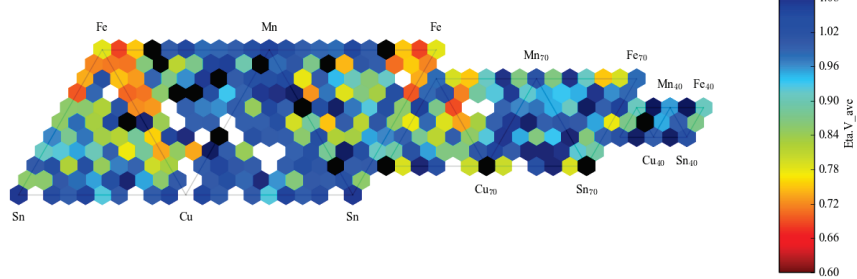
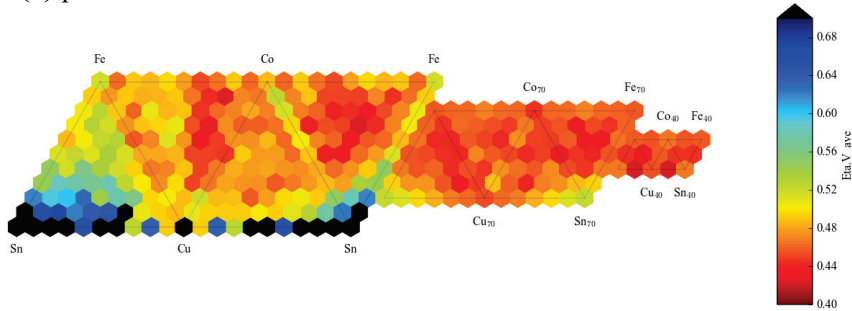
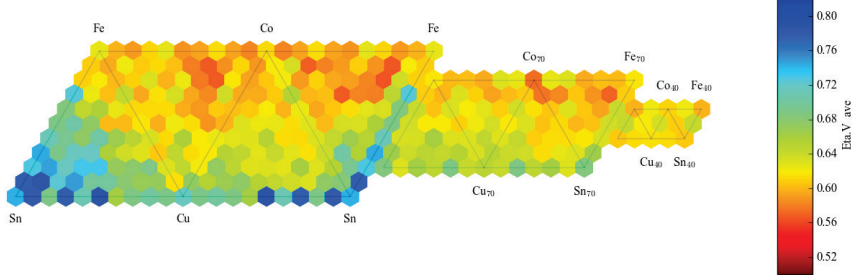


Figure S8-part 5. Composition map of η_{OER} at $10 \text{ mA}\cdot\text{cm}^{-2}$ for the pseudoquaternary (Sn-Fe-Cu-Mn)O_x in (a) pH 13, (b) pH 9, (c) pH 7, (d) pH 3 (note different color scale at each pH).

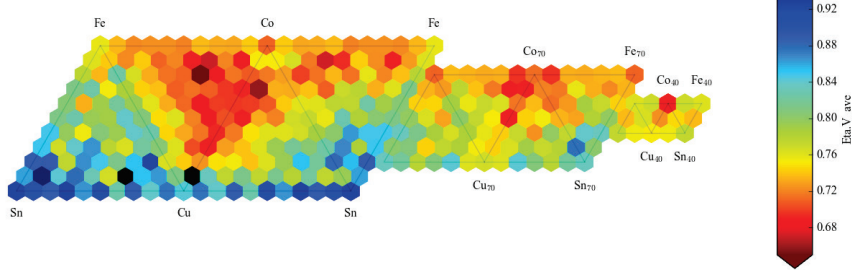
(a) pH 13



(b) pH 9



(c) pH 7



(d) pH 3

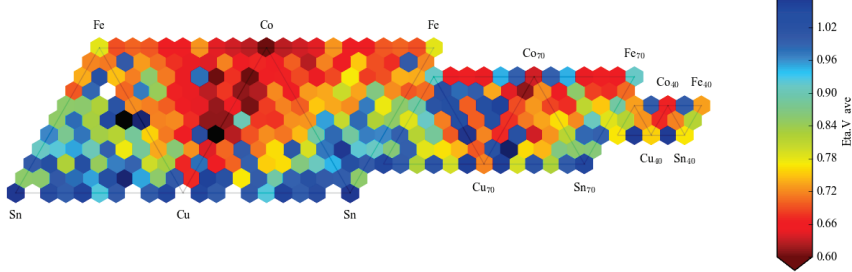
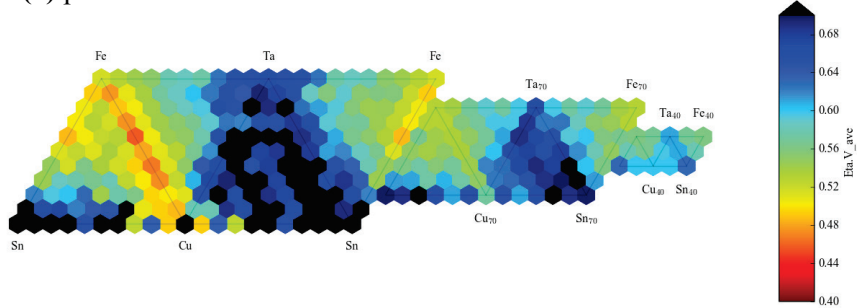
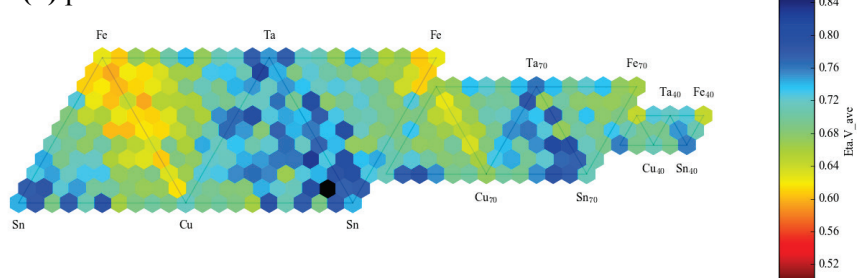


Figure S8-part 6. Composition map of η_{OER} at $10 \text{ mA}\cdot\text{cm}^{-2}$ for the pseudoquaternary (Sn-Fe-Cu-Co)O_x in (a) pH 13, (b) pH 9, (c) pH 7, (d) pH 3 (note different color scale at each pH).

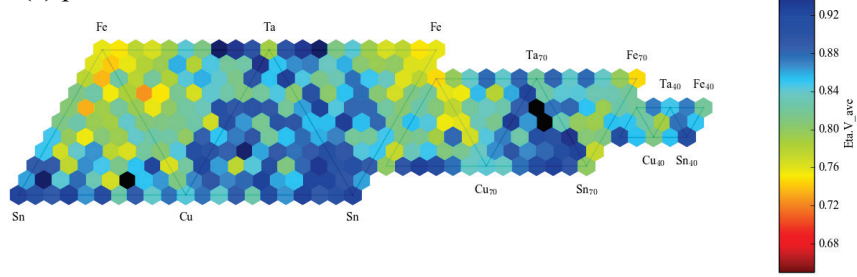
(a) pH 13



(b) pH 9



(c) pH 7



(d) pH 3

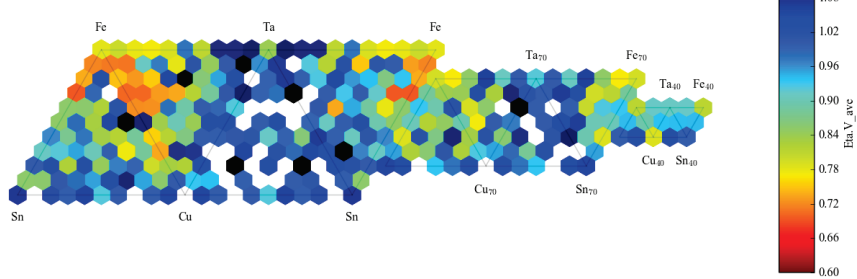
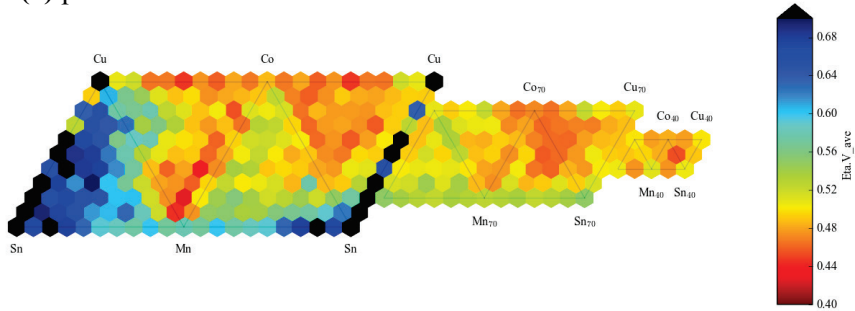
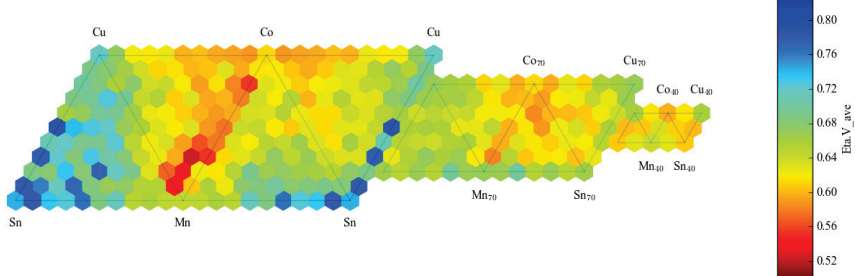


Figure S8-part 7. Composition map of η_{OER} at $10 \text{ mA}\cdot\text{cm}^{-2}$ for the pseudoquaternary $(\text{Sn}-\text{Fe}-\text{Cu}-\text{Ta})\text{O}_x$ in (a) pH 13, (b) pH 9, (c) pH 7, (d) pH 3 (note different color scale at each pH).

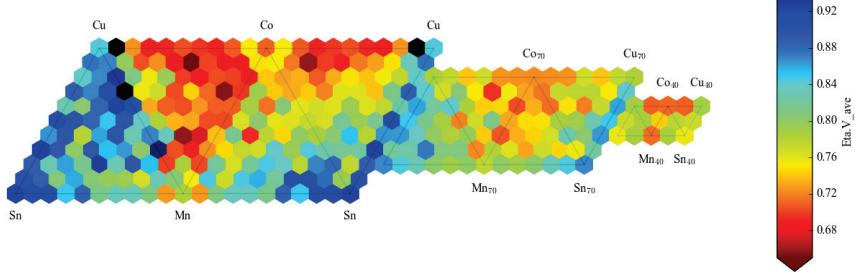
(a) pH 13



(b) pH 9



(c) pH 7



(d) pH 3

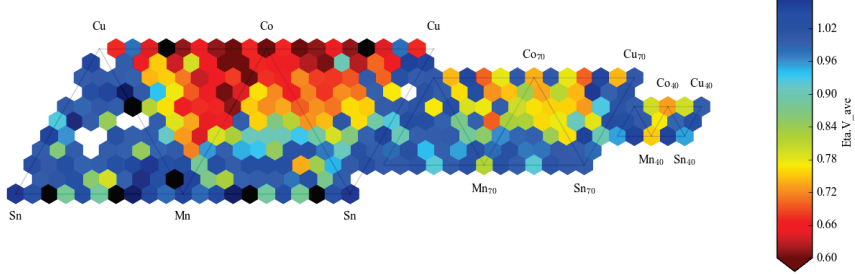
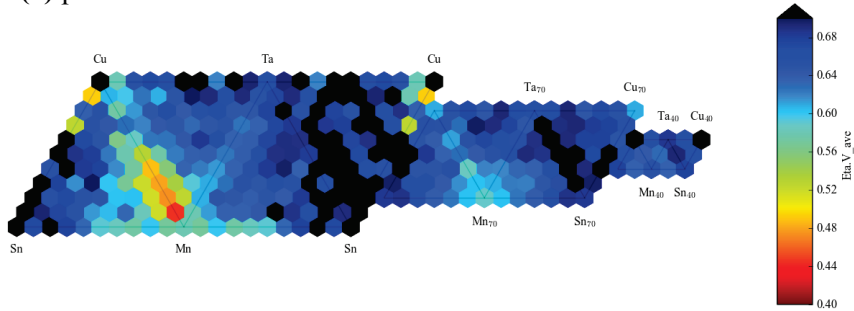
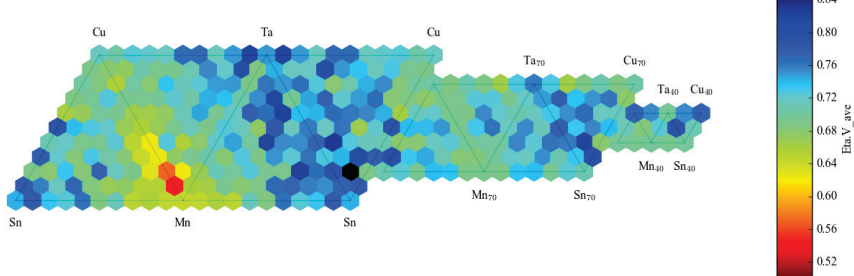


Figure S8-part 8. Composition map of η_{OER} at $10 \text{ mA}\cdot\text{cm}^{-2}$ for the pseudoquaternary $(\text{Sn}-\text{Cu}-\text{Mn}-\text{Co})\text{O}_x$ in (a) pH 13, (b) pH 9, (c) pH 7, (d) pH 3 (note different color scale at each pH).

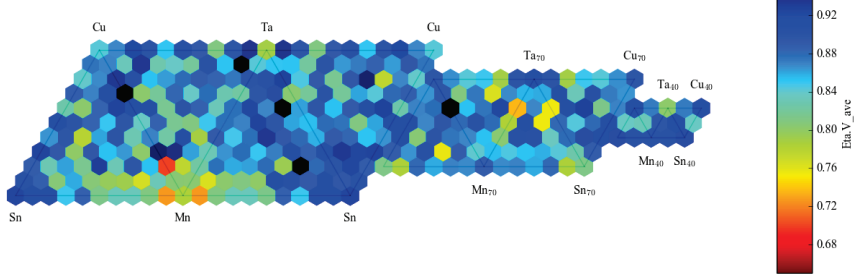
(a) pH 13



(b) pH 9



(c) pH 7



(d) pH 3

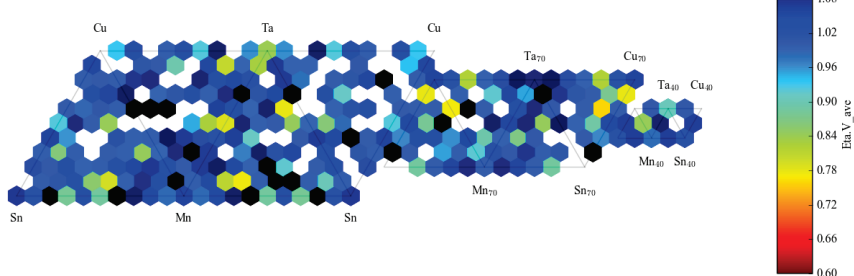
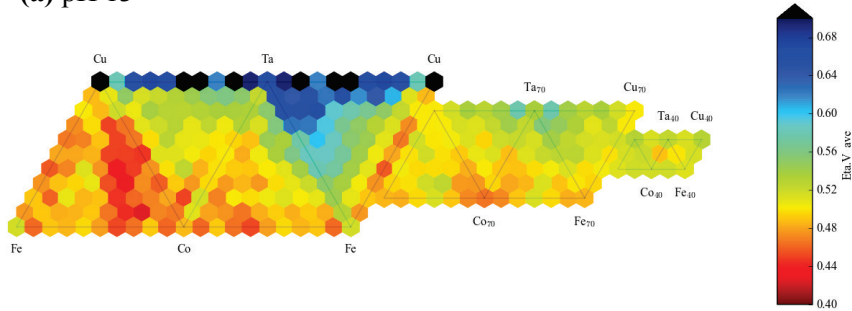
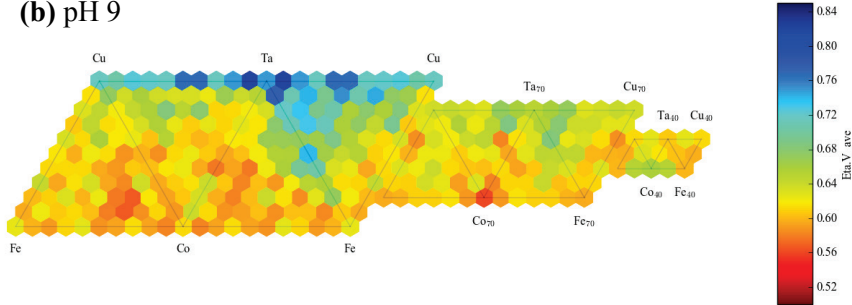


Figure S8-part 9. Composition map of η_{OER} at $10 \text{ mA}\cdot\text{cm}^{-2}$ for the pseudoquaternary $(\text{Sn}-\text{Cu}-\text{Mn}-\text{Ta})\text{O}_x$ in (a) pH 13, (b) pH 9, (c) pH 7, (d) pH 3 (note different color scale at each pH).

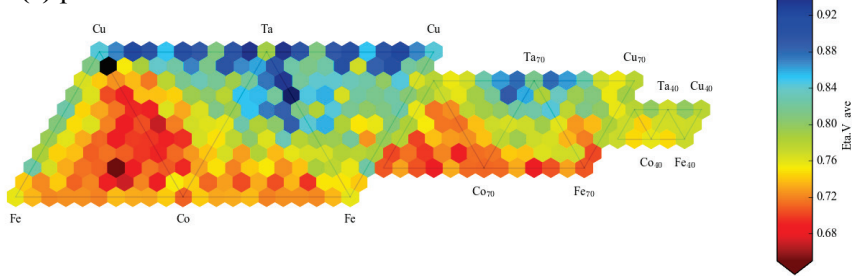
(a) pH 13



(b) pH 9



(c) pH 7



(d) pH 3

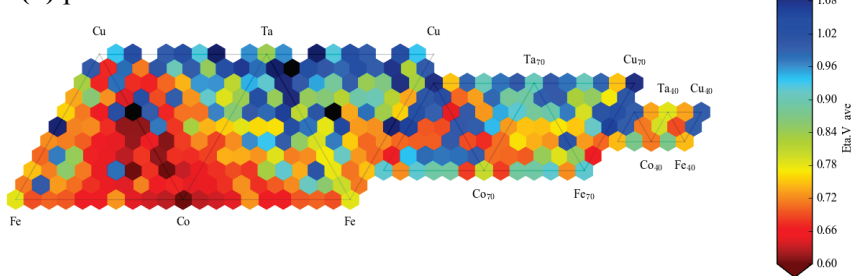
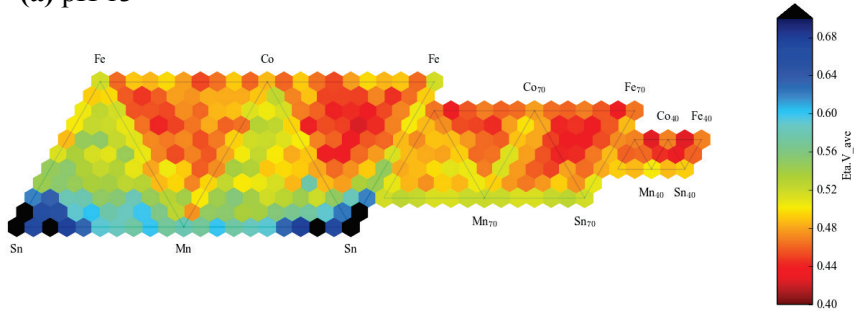
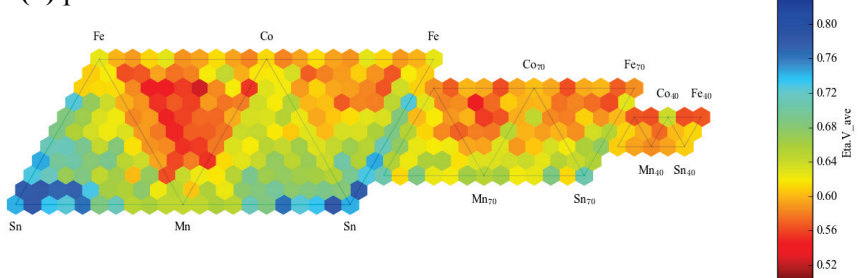


Figure S8-part 10. Composition map of η_{OER} at $10 \text{ mA}\cdot\text{cm}^{-2}$ for the pseudoquaternary $(\text{Fe}-\text{Cu}-\text{Co}-\text{Ta})\text{O}_x$ in (a) pH 13, (b) pH 9, (c) pH 7, (d) pH 3 (note different color scale at each pH).

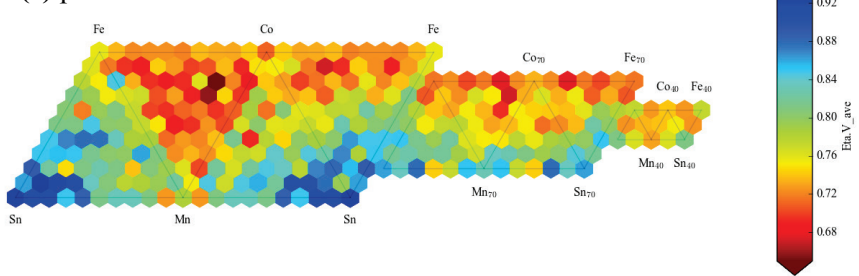
(a) pH 13



(b) pH 9



(c) pH 7



(d) pH 3

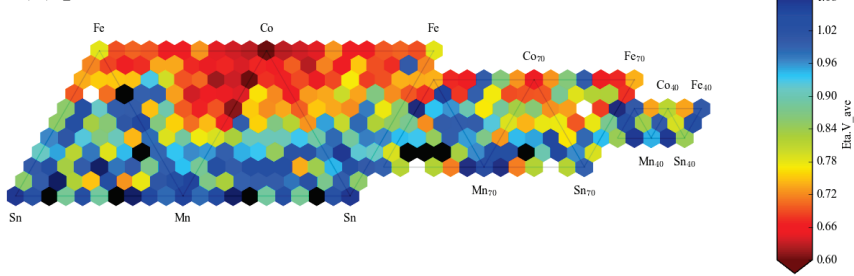
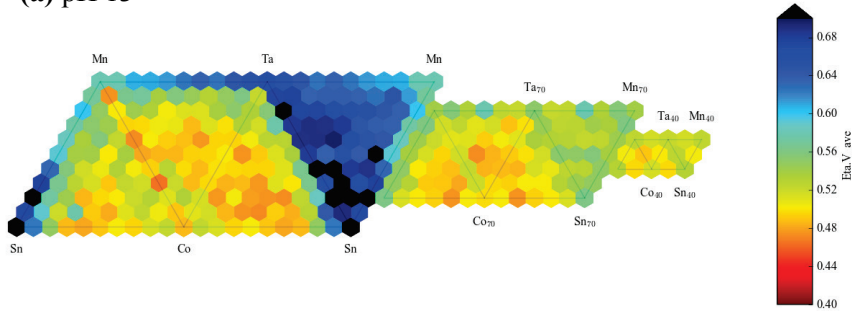
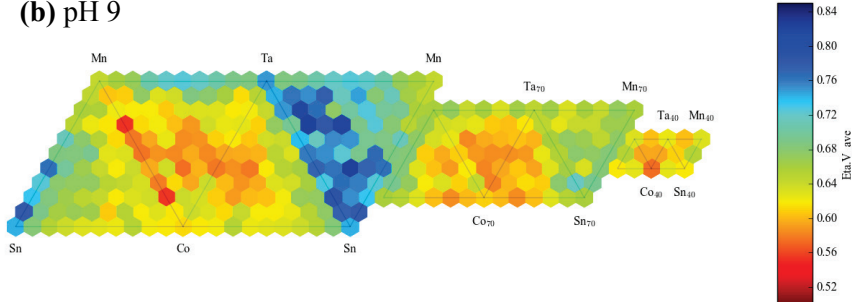


Figure S8-part 11. Composition map of η_{OER} at $10 \text{ mA}\cdot\text{cm}^{-2}$ for the pseudoquaternary $(\text{Sn}-\text{Fe}-\text{Mn}-\text{Co})\text{O}_x$ in (a) pH 13, (b) pH 9, (c) pH 7, (d) pH 3 (note different color scale at each pH).

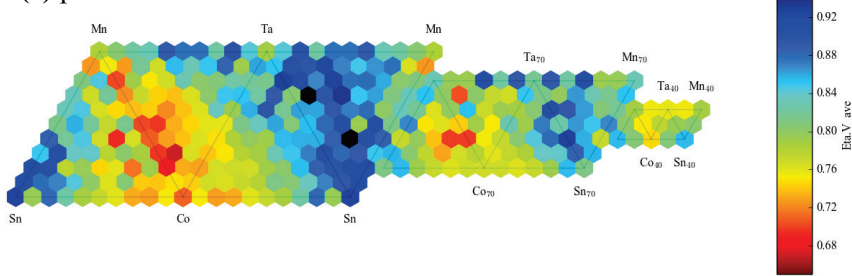
(a) pH 13



(b) pH 9



(c) pH 7



(d) pH 3

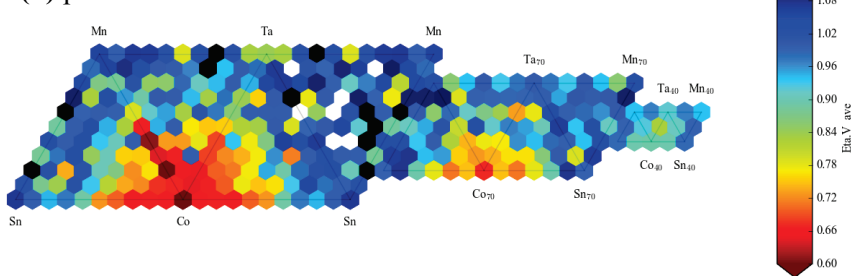
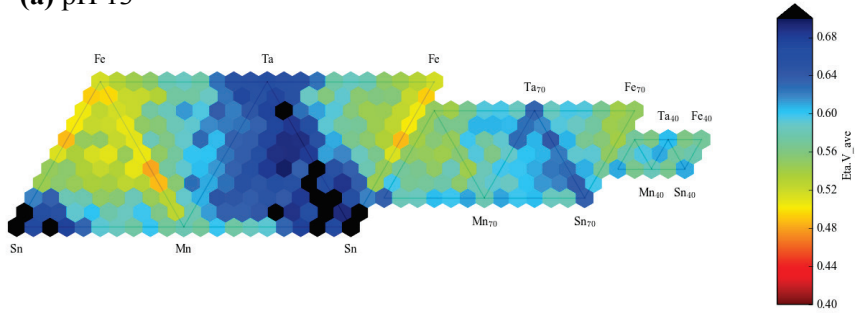
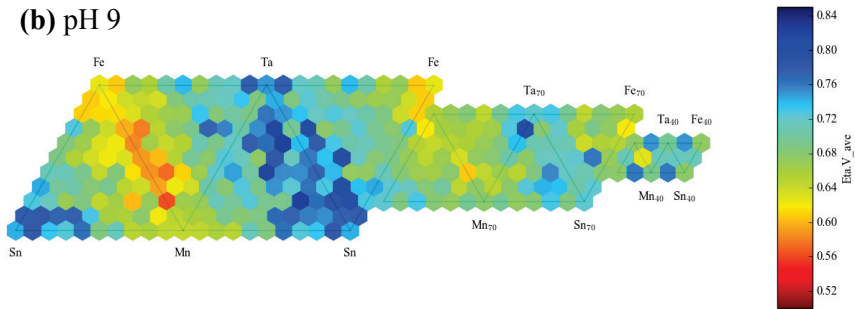


Figure S8-part 12. Composition map of η_{OER} at $10 \text{ mA}\cdot\text{cm}^{-2}$ for the pseudoquaternary $(\text{Sn}-\text{Mn}-\text{Co}-\text{Ta})\text{O}_x$ in (a) pH 13, (b) pH 9, (c) pH 7, (d) pH 3 (note different color scale at each pH).

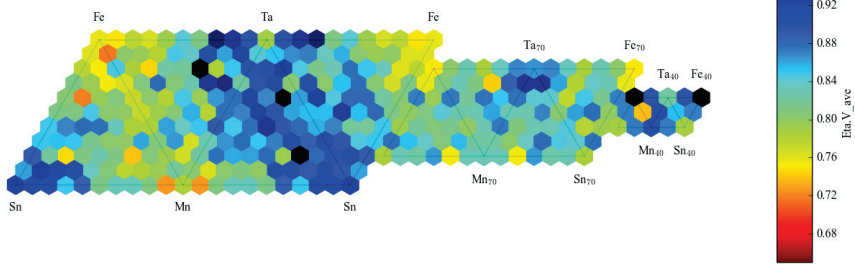
(a) pH 13



(b) pH 9



(c) pH 7



(d) pH 3

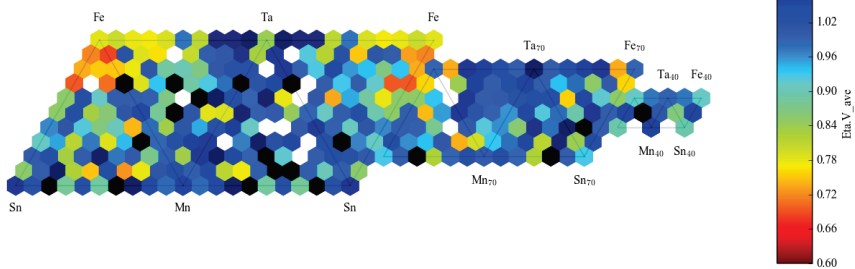
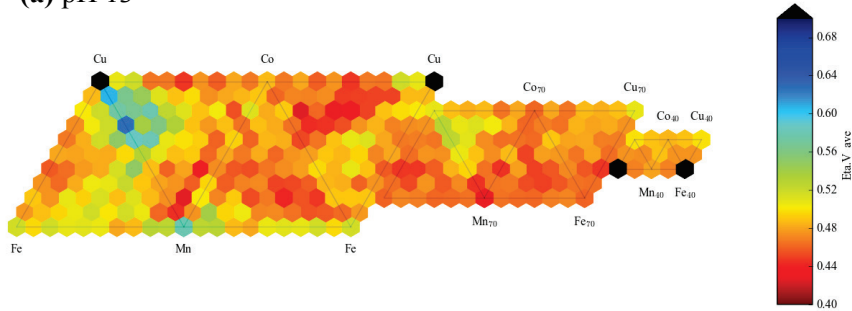
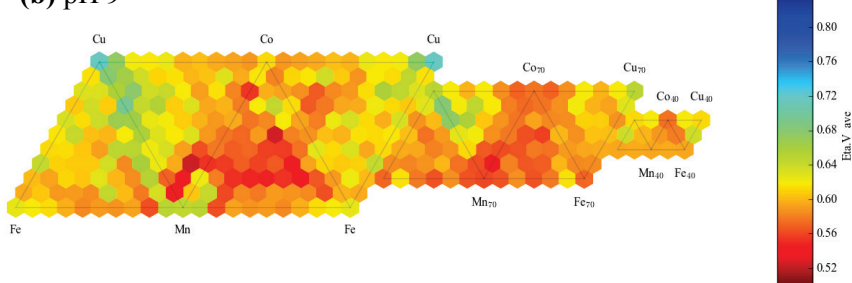


Figure S8-part 13. Composition map of η_{OER} at $10 \text{ mA}\cdot\text{cm}^{-2}$ for the pseudoquaternary $(\text{Sn}-\text{Fe}-\text{Mn}-\text{Ta})\text{O}_x$ in (a) pH 13, (b) pH 9, (c) pH 7, (d) pH 3 (note different color scale at each pH).

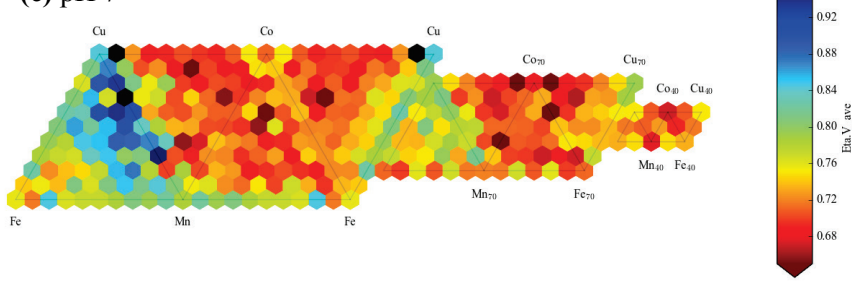
(a) pH 13



(b) pH 9



(c) pH 7



(d) pH 3

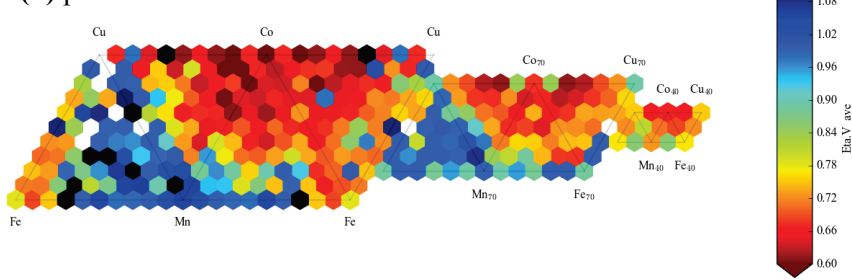
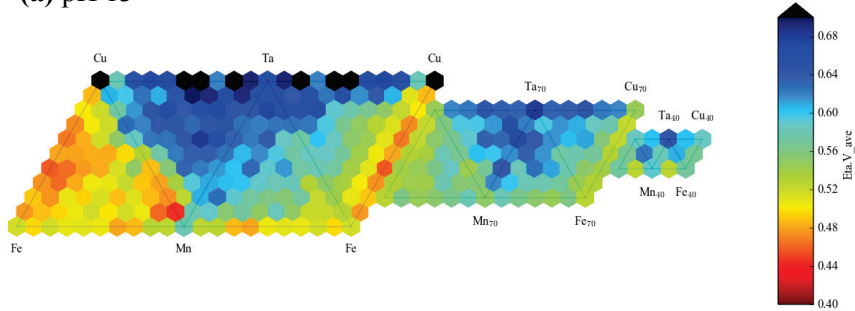
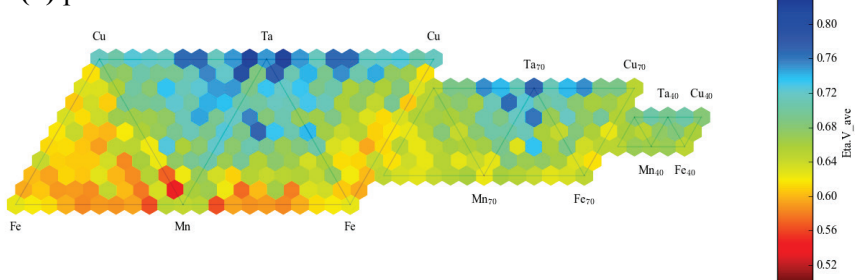


Figure S8-part 14. Composition map of η_{OER} at $10 \text{ mA}\cdot\text{cm}^{-2}$ for the pseudoquaternary $(\text{Fe}-\text{Cu}-\text{Mn}-\text{Co})\text{O}_x$ in (a) pH 13, (b) pH 9, (c) pH 7, (d) pH 3 (note different color scale at each pH).

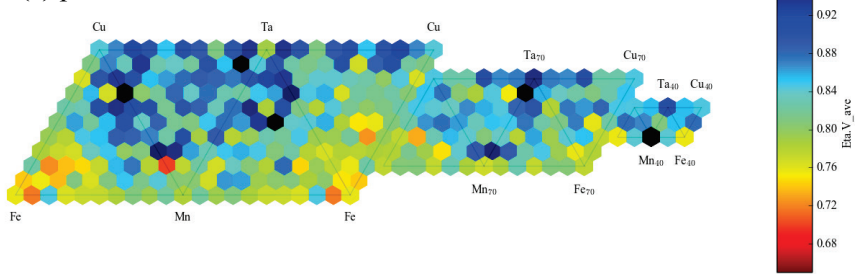
(a) pH 13



(b) pH 9



(c) pH 7



(d) pH 3

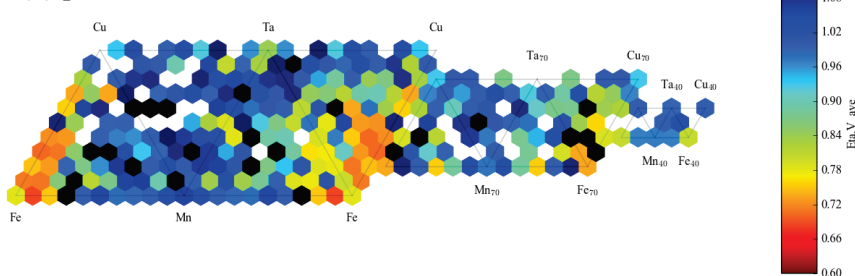
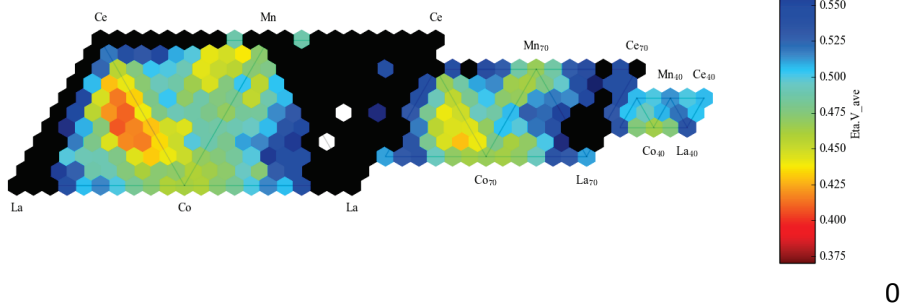
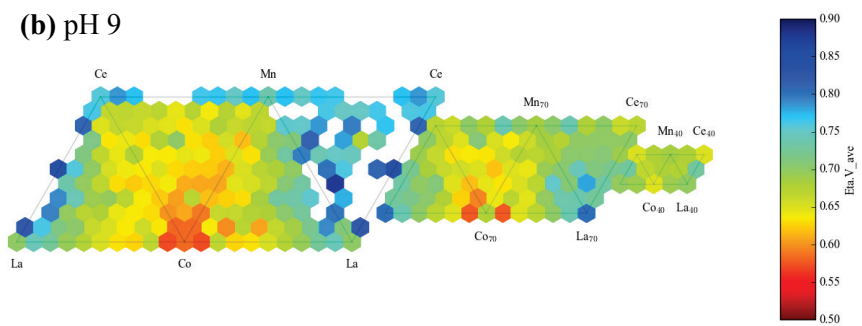


Figure S8-part 15. Composition map of η_{OER} at $10 \text{ mA}\cdot\text{cm}^{-2}$ for the pseudoquaternary $(\text{Fe}-\text{Cu}-\text{Mn}-\text{Ta})\text{O}_x$ in (a) pH 13, (b) pH 9, (c) pH 7, (d) pH 3 (note different color scale at each pH).

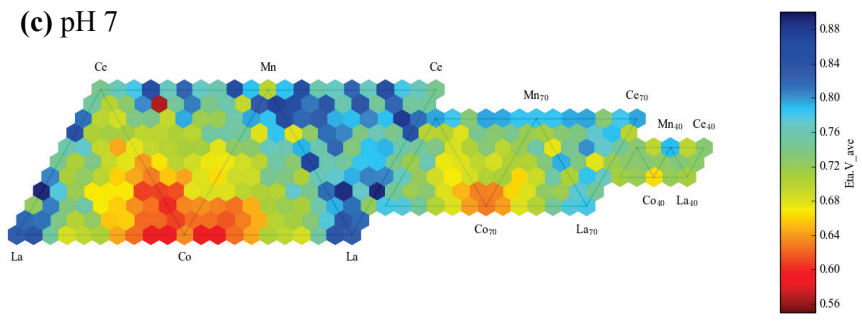
(a) pH 13



(b) pH 9



(c) pH 7



(d) pH 3

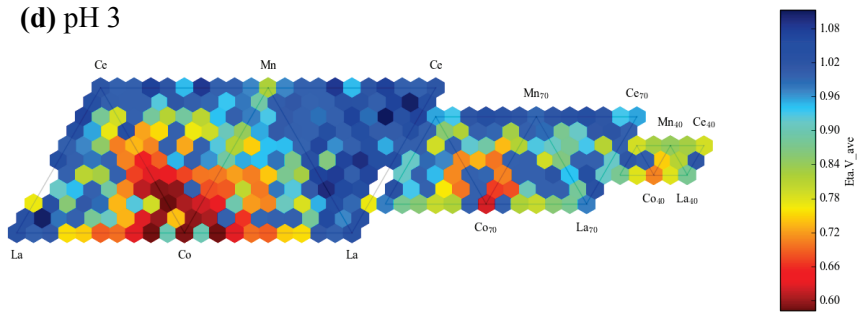
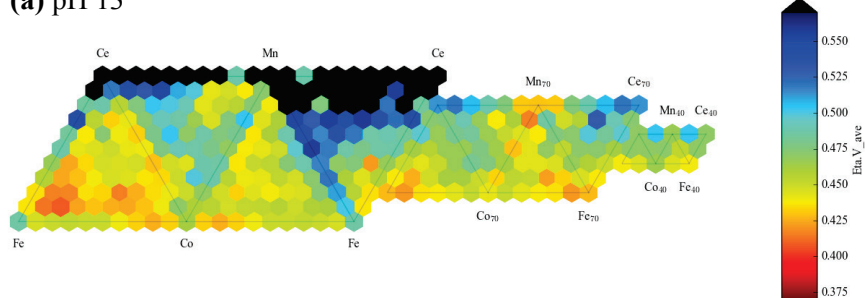
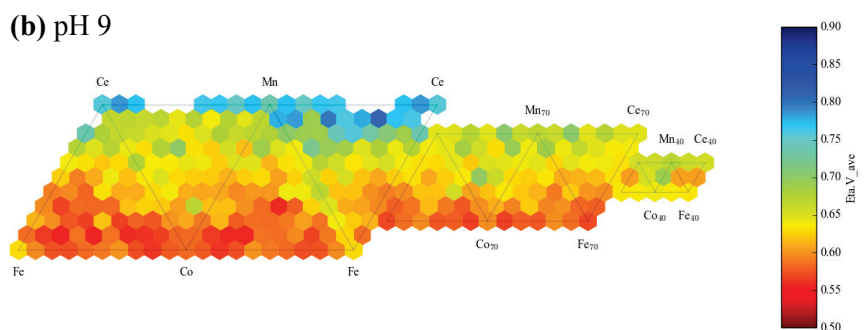


Figure S9-part 1. Composition maps from the (Ni-Fe-La-Ce-Co-Mn)O_x composition space: map of η_{OER} at 10 mA cm⁻² for the pseudoquaternary (La-Ce-Co-Mn)O_x in (a) pH 13, (b) pH 9, (c) pH 7, (d) pH 3 (note different color scale at each pH).

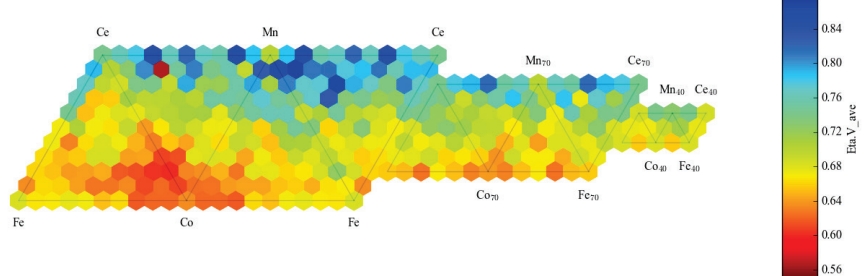
(a) pH 13



(b) pH 9



(c) pH 7



(d) pH 3

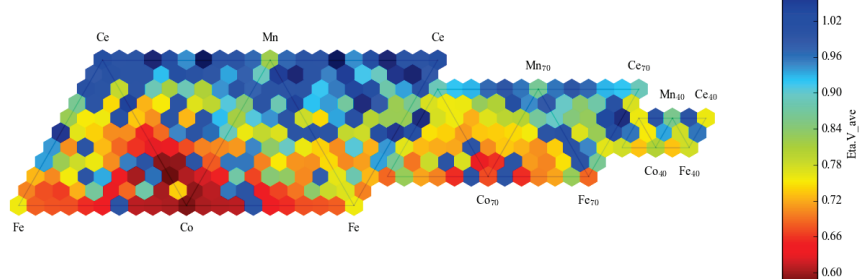
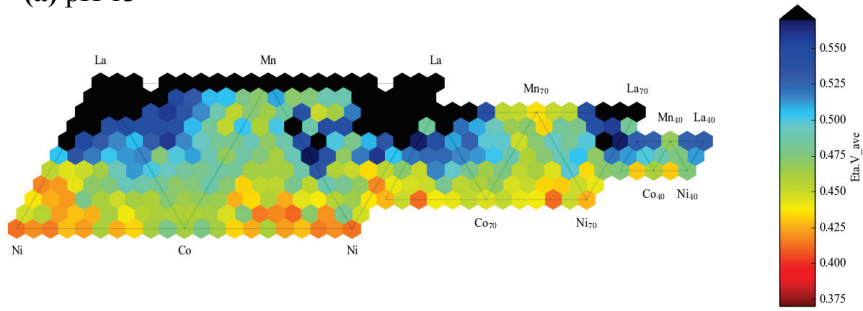
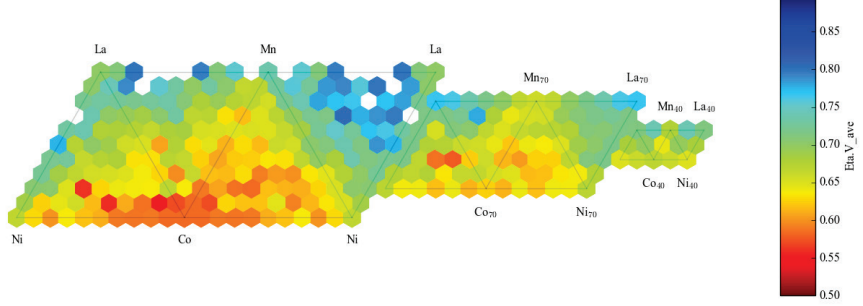


Figure S9-part 2. Composition maps from the (Ni-Fe-La-Ce-Co-Mn)O_x composition space: map of η_{OER} at 10 mA cm⁻² for the pseudoquaternary (Fe-Ce-Co-Mn)O_x in (a) pH 13, (b) pH 9, (c) pH 7, (d) pH 3 (note different color scale at each pH).

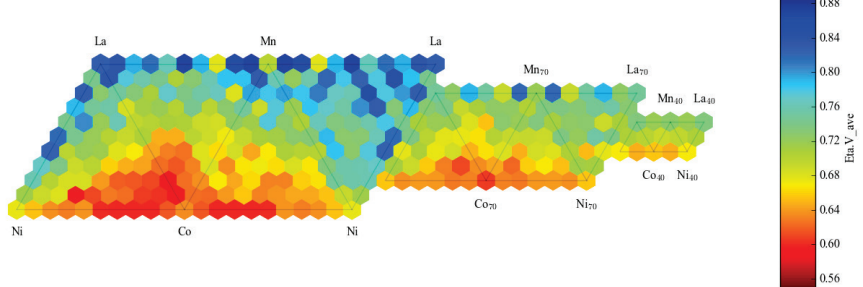
(a) pH 13



(b) pH 9



(c) pH 7



(d) pH 3

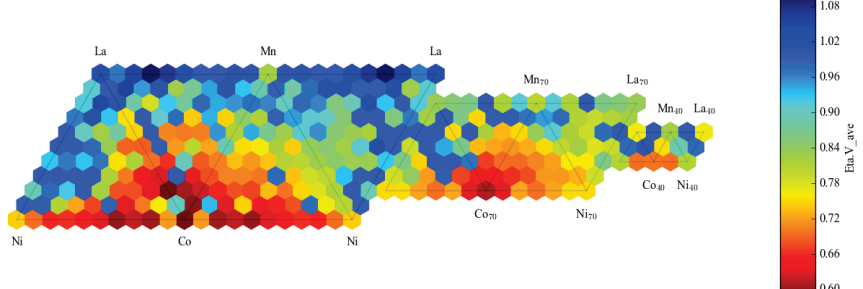
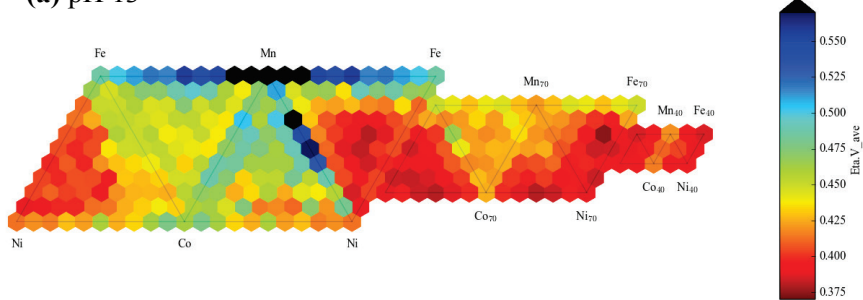
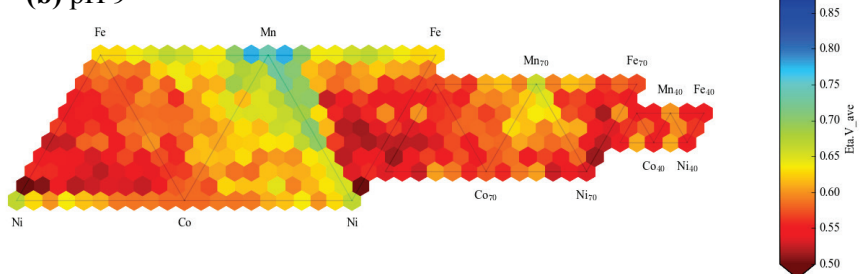


Figure S9-part 3. Composition maps from the (Ni-Fe-La-Ce-Co-Mn)O_x composition space: map of η_{OER} at 10 mA cm⁻² for the pseudoquaternary (Ni-La-Co-Mn)O_x in (a) pH 13, (b) pH 9, (c) pH 7, (d) pH 3 (note different color scale at each pH).

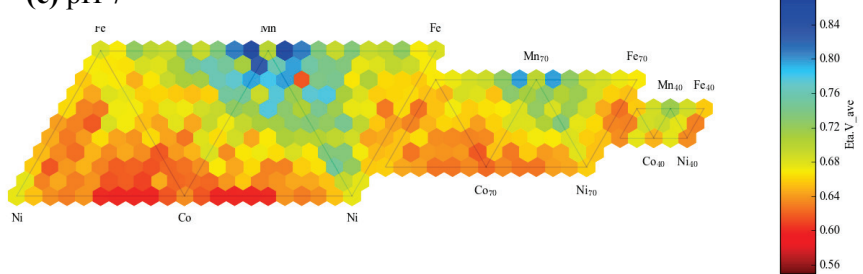
(a) pH 13



(b) pH 9



(c) pH 7



(d) pH 3

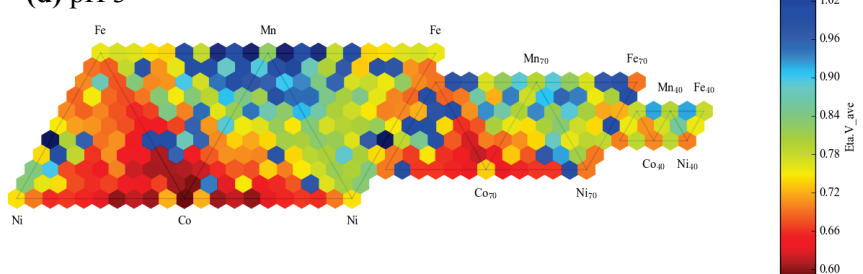
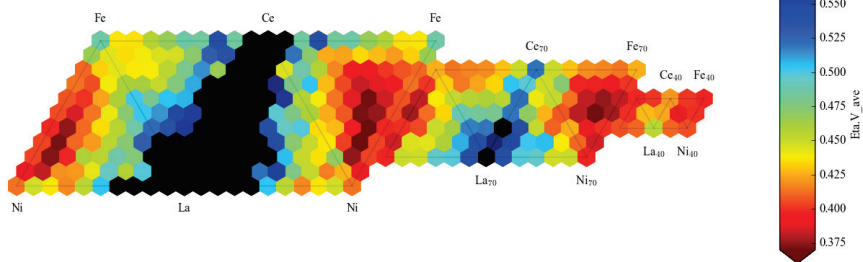
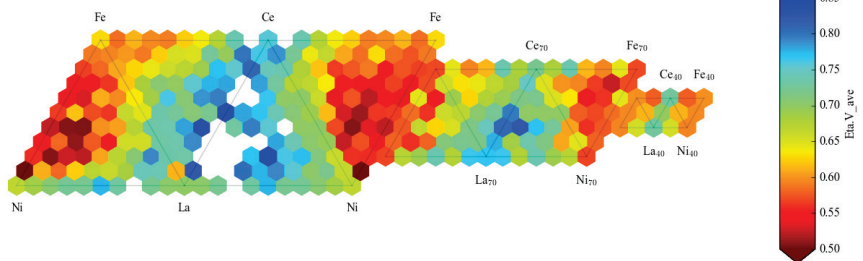


Figure S9-part 4. Composition maps from the (Ni-Fe-La-Ce-Co-Mn)O_x composition space: map of η_{OER} at 10 mA cm⁻² for the pseudoquaternary (Ni-Fe-Co-Mn)O_x in (a) pH 13, (b) pH 9, (c) pH 7, (d) pH 3 (note different color scale at each pH).

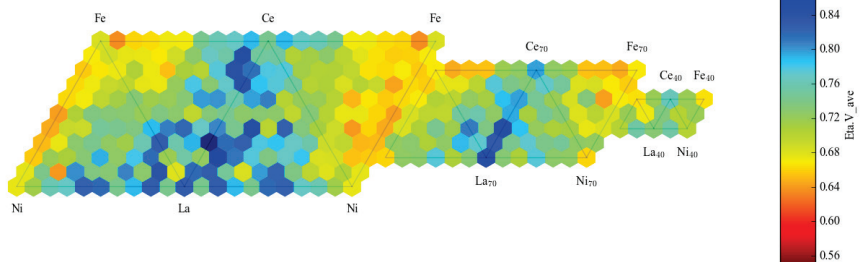
(a) pH 13



(b) pH 9



(c) pH 7



(d) pH 3

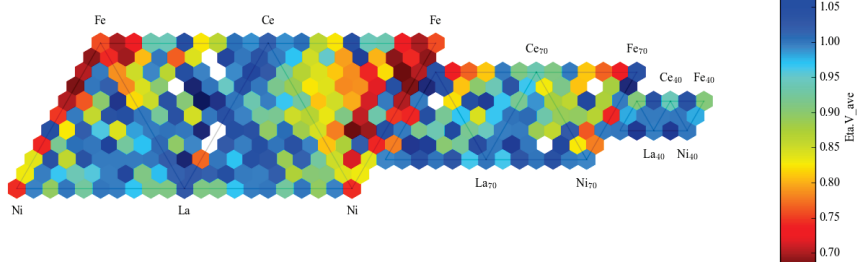
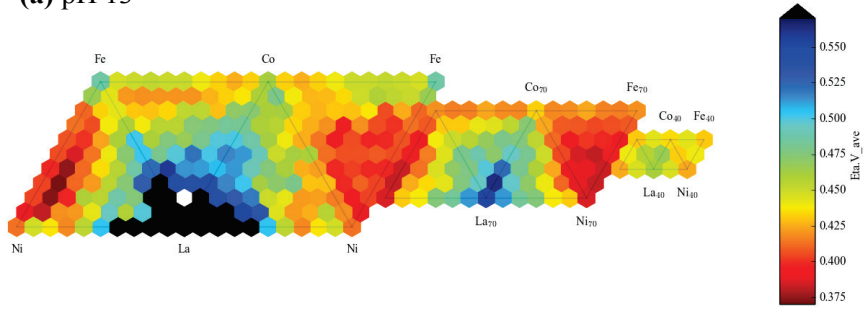
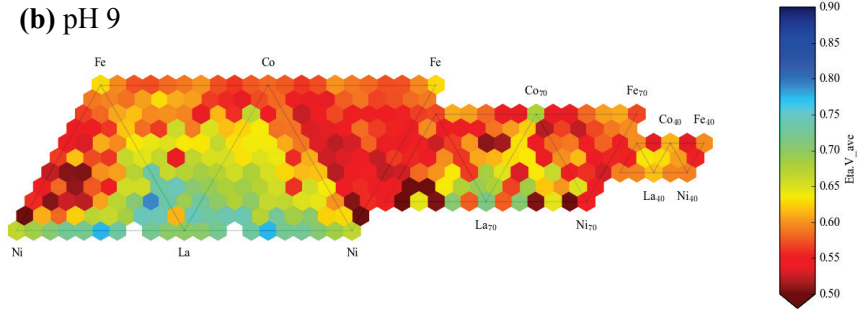


Figure S9-part 5. Composition maps from the (Ni-Fe-La-Ce-Co-Mn)O_x composition space: map of η_{OER} at 10 mA cm⁻² for the pseudoquaternary (Ni-Fe-La-Co)O_x in (a) pH 13, (b) pH 9, (c) pH 7, (d) pH 3 (note different color scale at each pH).

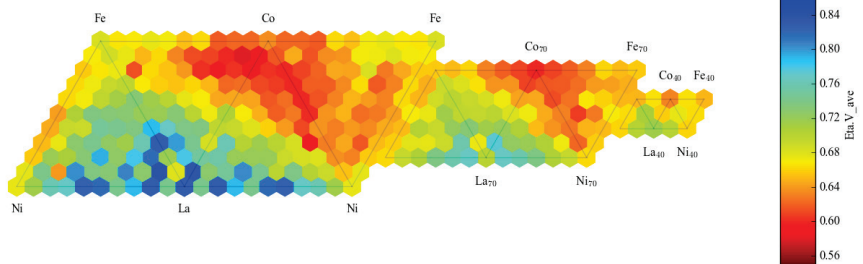
(a) pH 13



(b) pH 9



(c) pH 7



(d) pH 3

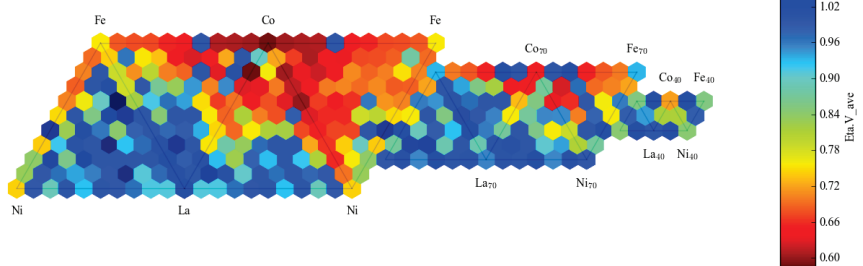
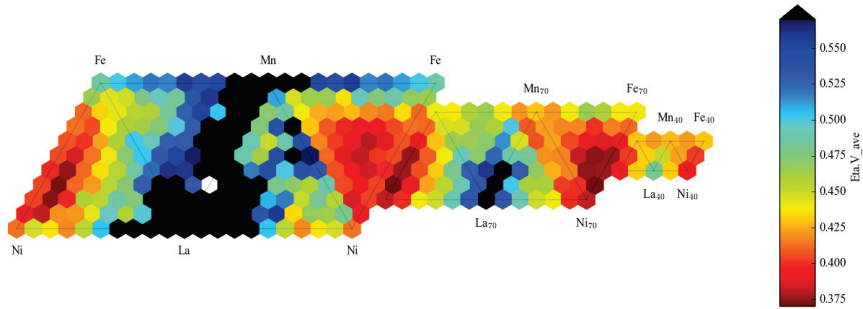
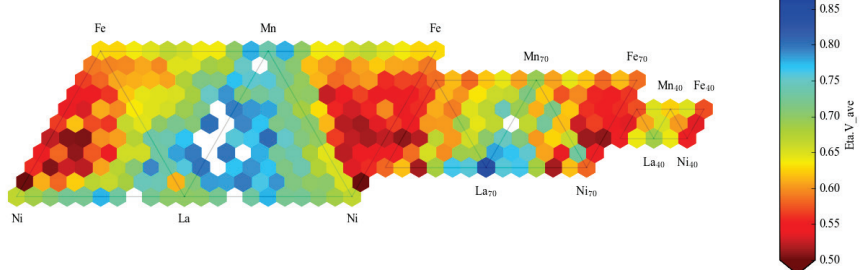


Figure S9-part 6. Composition maps from the (Ni-Fe-La-Ce-Co-Mn)O_x composition space: map of η_{OER} at 10 mA cm⁻² for the pseudoquaternary (Ni-Fe-La-Co)O_x in (a) pH 13, (b) pH 9, (c) pH 7, (d) pH 3 (note different color scale at each pH).

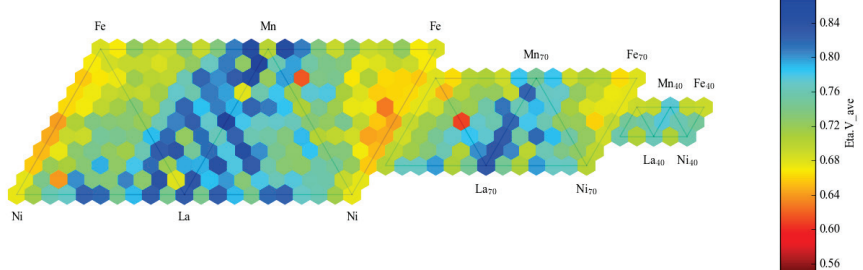
(a) pH 13



(b) pH 9



(c) pH 7



(d) pH 3

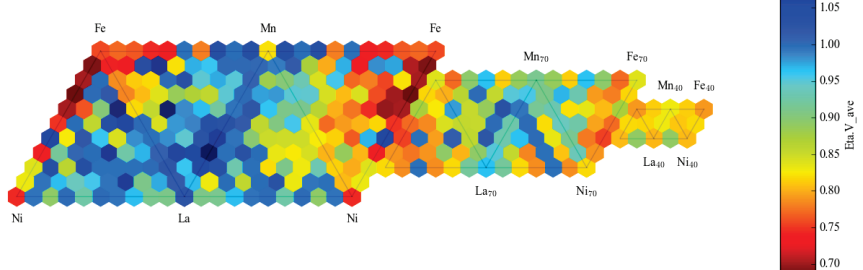
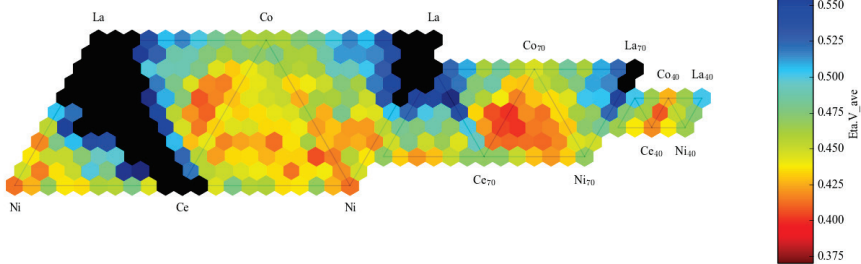
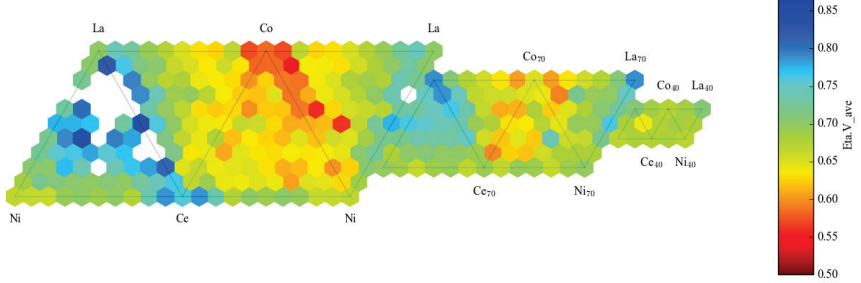


Figure S9-part 7. Composition maps from the (Ni-Fe-La-Ce-Co-Mn)O_x composition space: map of η_{OER} at 10 mA cm⁻² for the pseudoquaternary (Ni-Fe-La-Mn)O_x in (a) pH 13, (b) pH 9, (c) pH 7, (d) pH 3 (note different color scale at each pH).

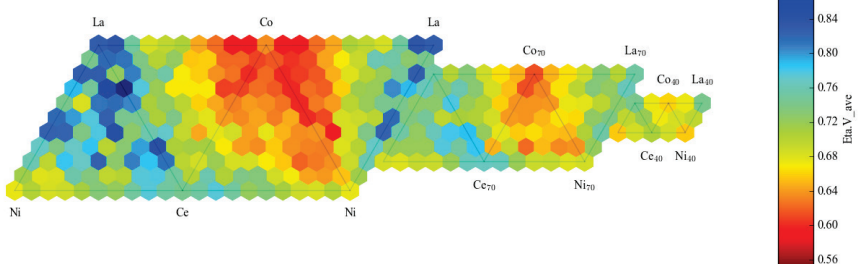
(a) pH 13



(b) pH 9



(c) pH 7



(d) pH 3

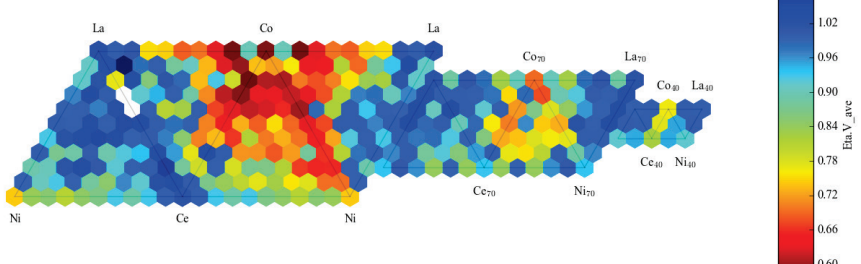
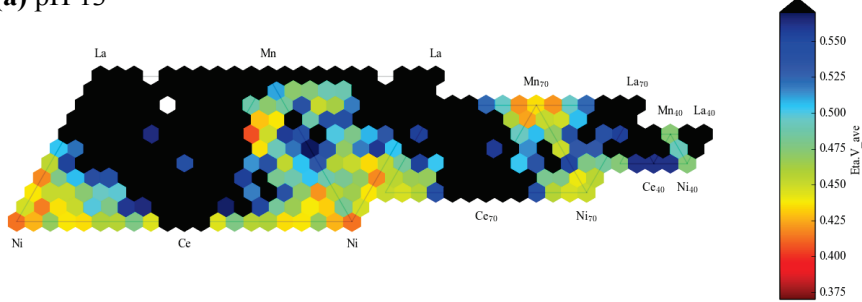
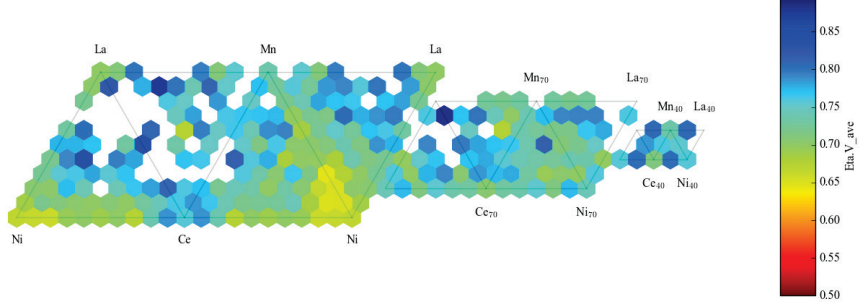


Figure S9-part 8. Composition maps from the (Ni-Fe-La-Ce-Co-Mn)O_x composition space: map of η_{OER} at 10 mA cm⁻² for the pseudoquaternary (Ni-La-Ce-Co)O_x in (a) pH 13, (b) pH 9, (c) pH 7, (d) pH 3 (note different color scale at each pH).

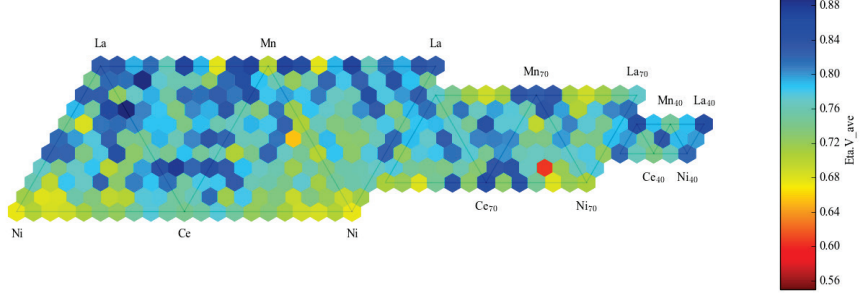
(a) pH 13



(b) pH 9



(c) pH 7



(d) pH 3

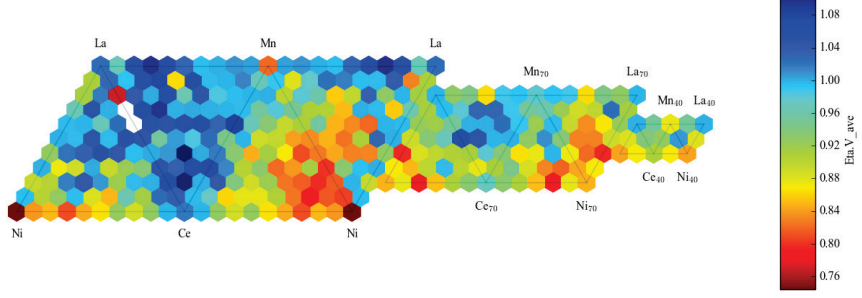
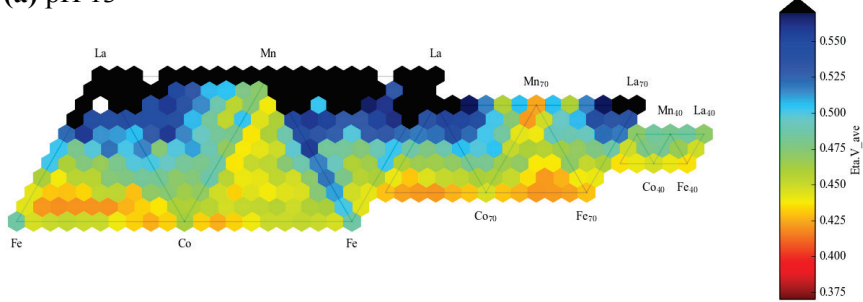
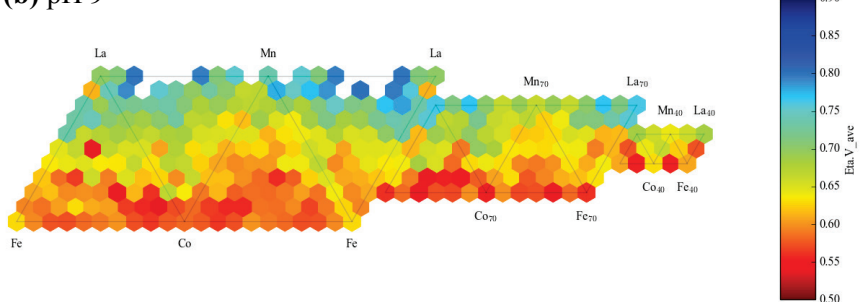


Figure S9-part 9. Composition maps from the (Ni-Fe-La-Ce-Co-Mn)O_x composition space: map of η_{OER} at 10 mA cm⁻² for the pseudoquaternary (Ni-La-Ce-Mn)O_x in (a) pH 13, (b) pH 9, (c) pH 7, (d) pH 3 (note different color scale at each pH).

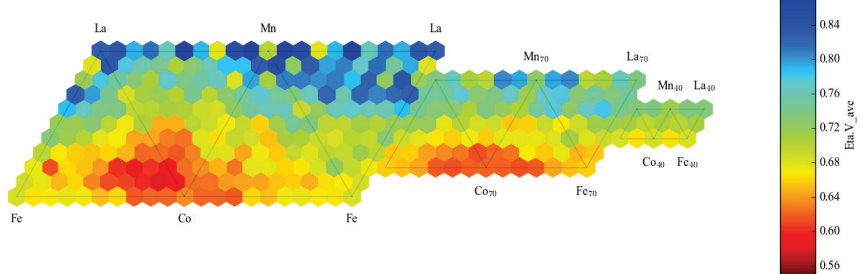
(a) pH 13



(b) pH 9



(c) pH 7



(d) pH 3

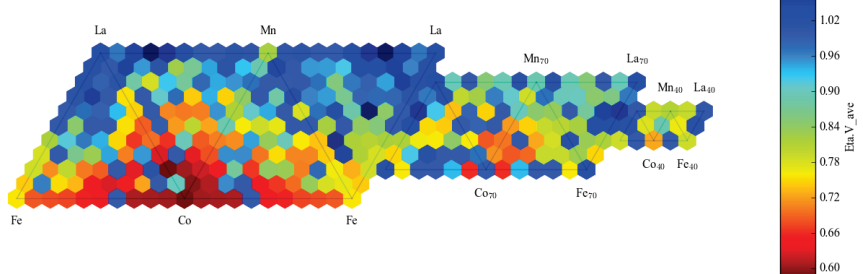
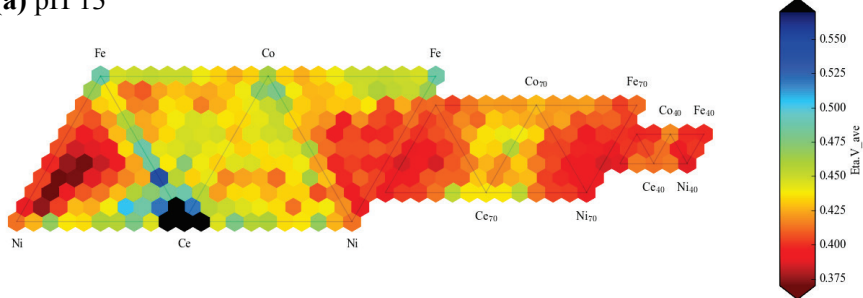
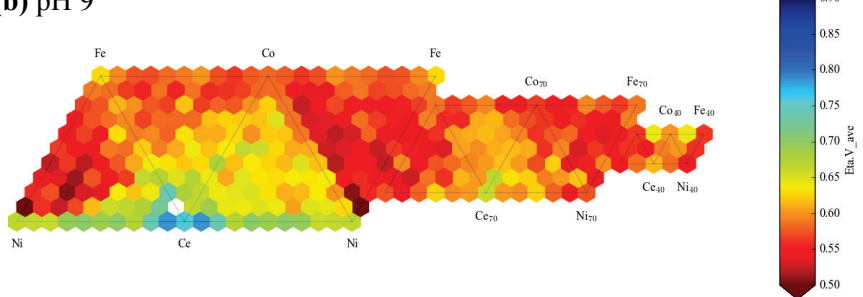


Figure S9-part 10. Composition maps from the (Ni-Fe-La-Ce-Co-Mn)O_x composition space: map of η_{OER} at 10 mA cm⁻² for the pseudoquaternary (Fe-La-Co-Mn)O_x in (a) pH 13, (b) pH 9, (c) pH 7, (d) pH 3 (note different color scale at each pH).

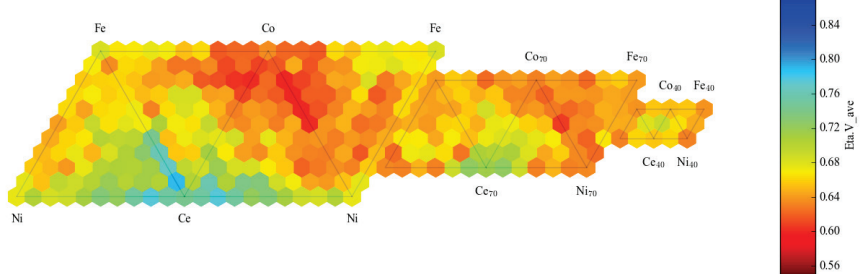
(a) pH 13



(b) pH 9



(c) pH 7



(d) pH 3

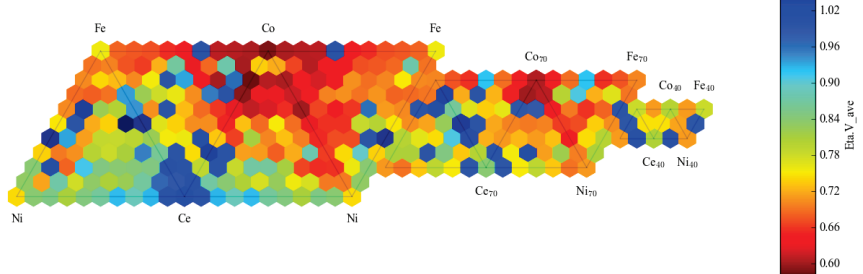
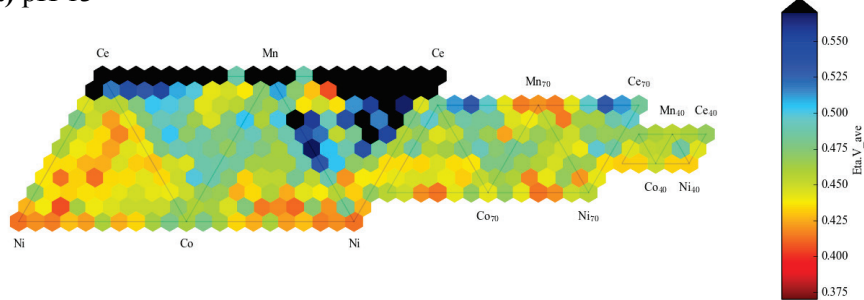
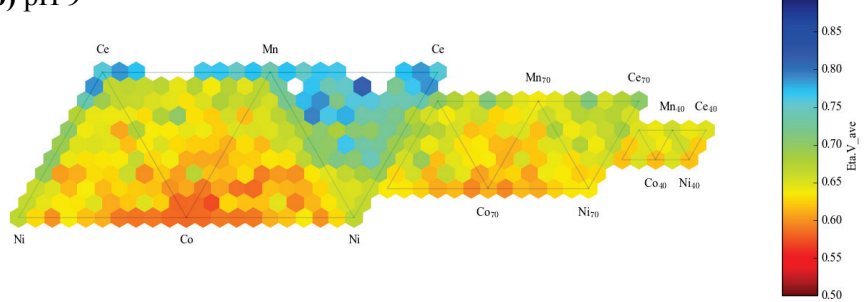


Figure S9-part 11. Composition maps from the (Ni-Fe-La-Ce-Co-Mn)O_x composition space: map of η_{OER} at 10 mA cm⁻² for the pseudoquaternary (Ni-Fe-Ce-Co)O_x in (a) pH 13, (b) pH 9, (c) pH 7, (d) pH 3 (note different color scale at each pH).

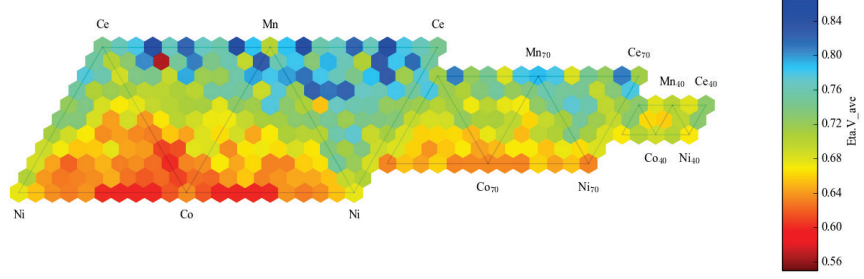
(a) pH 13



(b) pH 9



(c) pH 7



(d) pH 3

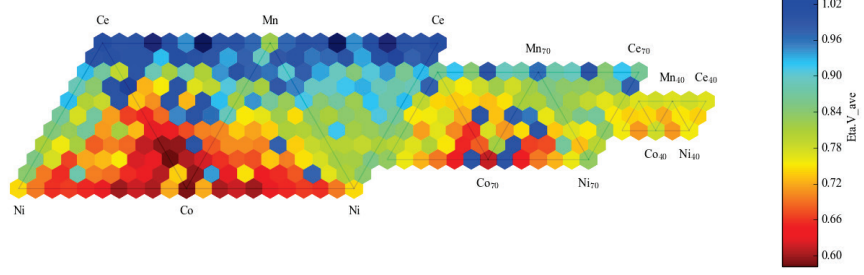
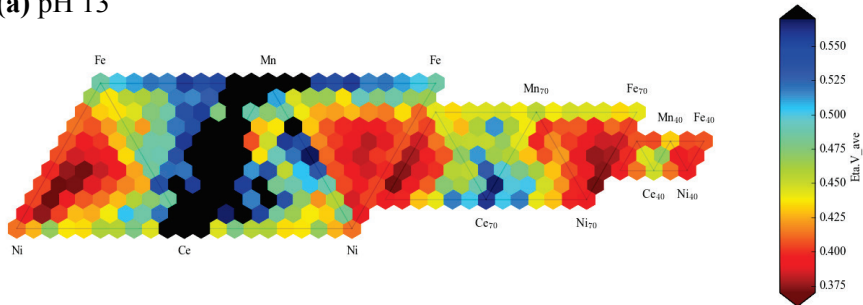
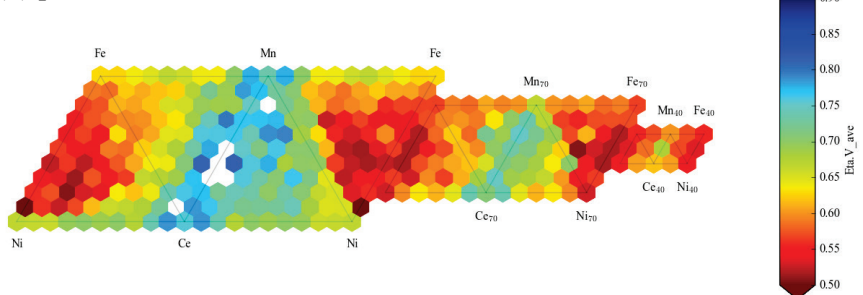


Figure S9-part 12. Composition maps from the (Ni-Fe-La-Ce-Co-Mn)O_x composition space: map of Η_{OER} at 10 mA cm⁻² for the pseudoquaternary (Ni-Ce-Co-Mn)O_x in (a) pH 13, (b) pH 9, (c) pH 7, (d) pH 3 (note different color scale at each pH).

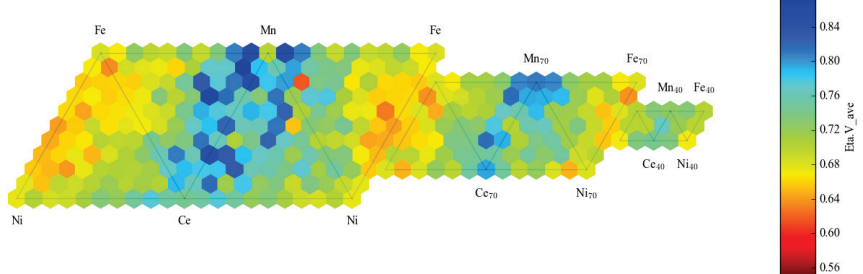
(a) pH 13



(b) pH 9



(c) pH 7



(d) pH 3

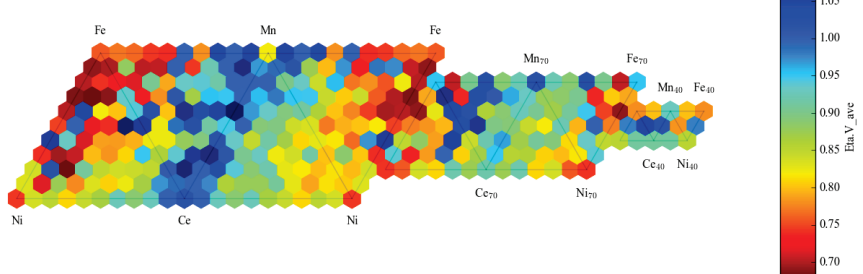
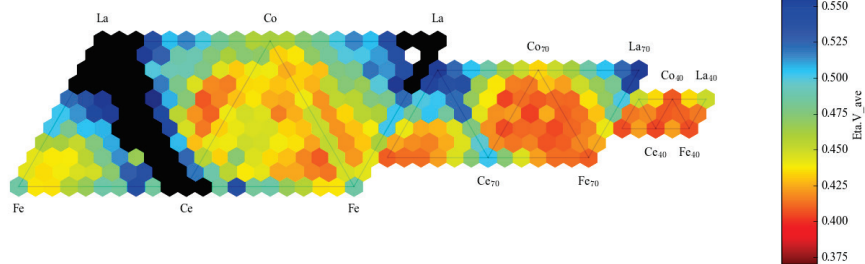
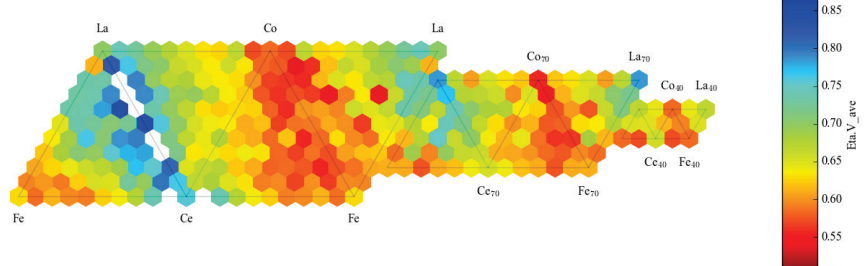


Figure S9-part 13. Composition maps from the (Ni-Fe-La-Ce-Co-Mn)O_x composition space: map of η_{OER} at 10 mA cm⁻² for the pseudoquaternary (Ni-Fe-Ce-Mn)O_x in (a) pH 13, (b) pH 9, (c) pH 7, (d) pH 3 (note different color scale at each pH).

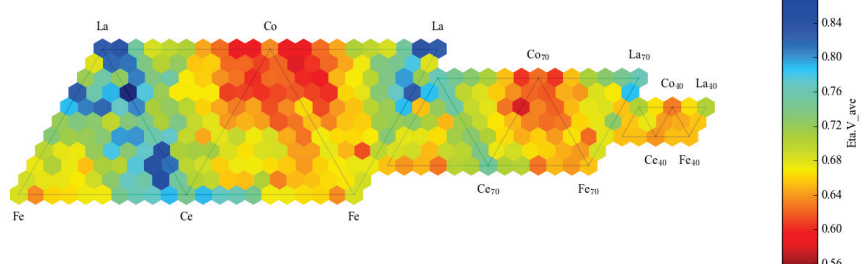
(a) pH 13



(b) pH 9



(c) pH 7



(d) pH 3

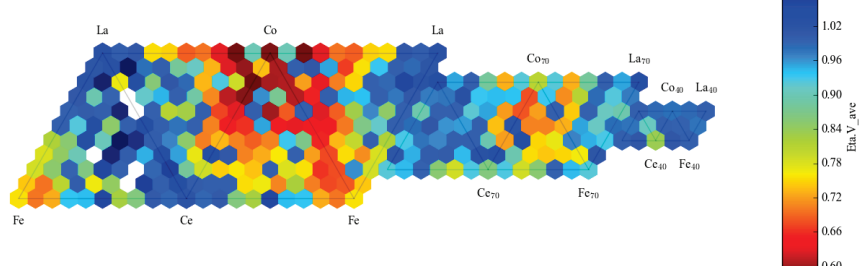
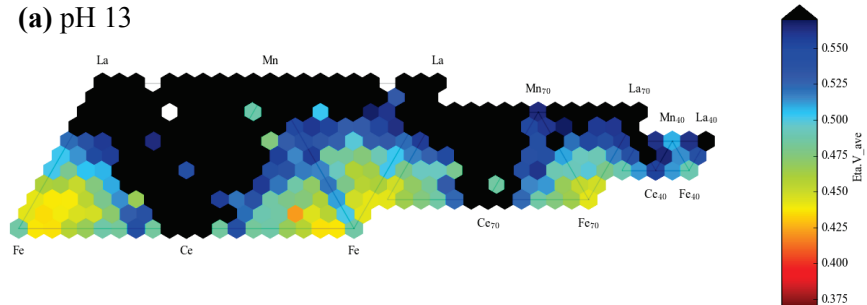
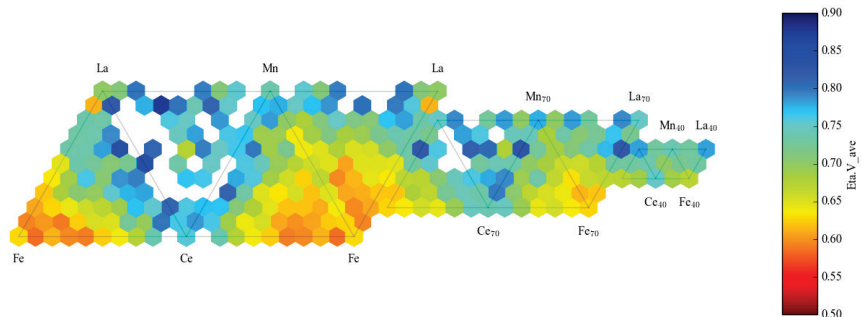


Figure S9-part 14. Composition maps from the (Ni-Fe-La-Ce-Co-Mn)O_x composition space: map of η_{OER} at 10 mA cm⁻² for the pseudoquaternary (Fe-La-Ce-Co)O_x in (a) pH 13, (b) pH 9, (c) pH 7, (d) pH 3 (note different color scale at each pH).

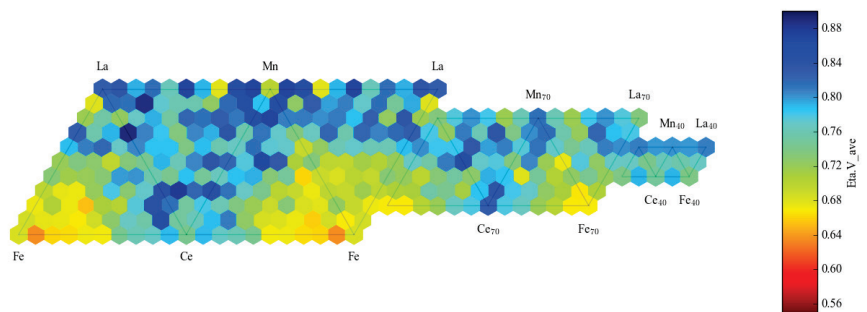
(a) pH 13



(b) pH 9



(c) pH 7



(d) pH 3

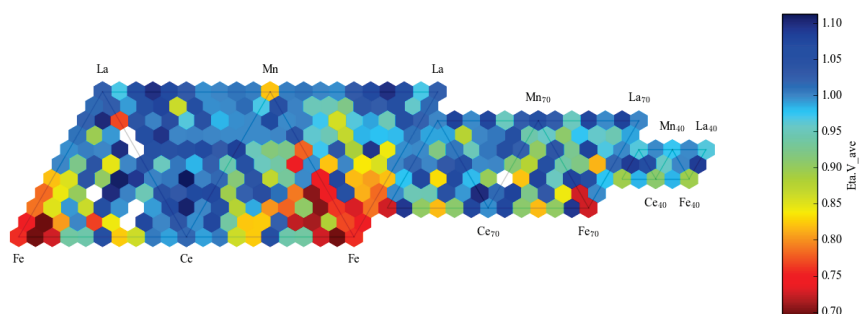
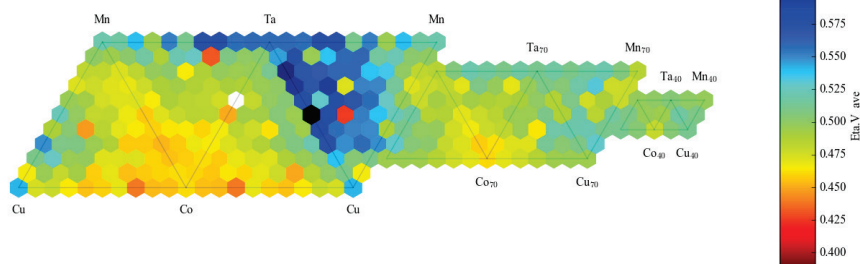
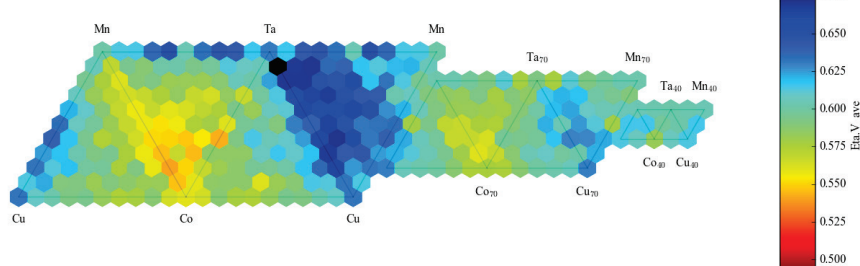


Figure S9-part 15. Composition maps from the (Ni-Fe-La-Ce-Co-Mn)O_x composition space: map of η_{OER} at 10 mA cm⁻² for the pseudoquaternary (Fe-La-Ce-Mn)O_x in (a) pH 13, (b) pH 9, (c) pH 7, (d) pH 3 (note different color scale at each pH).

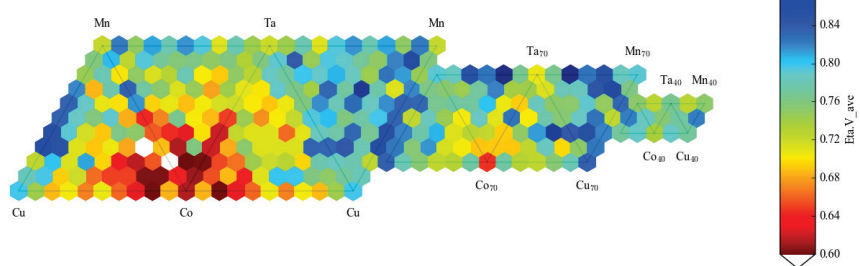
(a) pH 13



(b) pH 9



(c) pH 7



(d) pH 3

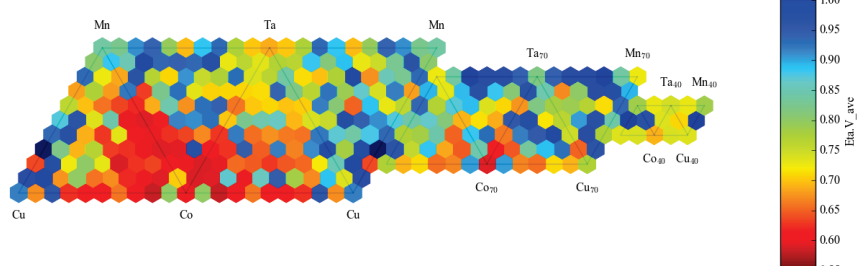
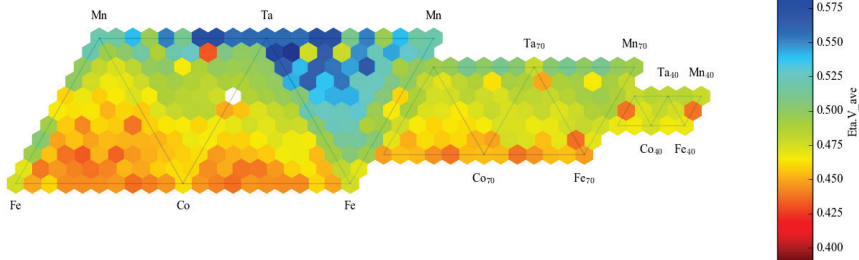
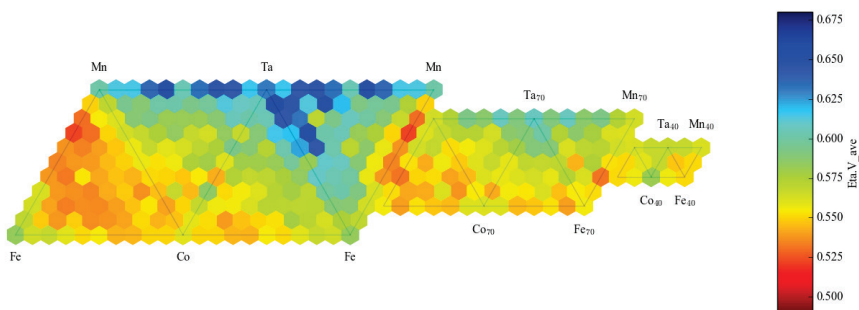


Figure S10-part 1. Composition maps from the (Ni-Fe-Cu-Mn-Co-Ta)O_x composition space: map of η_{OER} at 10 mA cm⁻² for the pseudoquaternary (Cu-Mn-Co-Ta)O_x in (a) pH 13, (b) pH 9, (c) pH 7, (d) pH 3 (note different color scale at each pH).

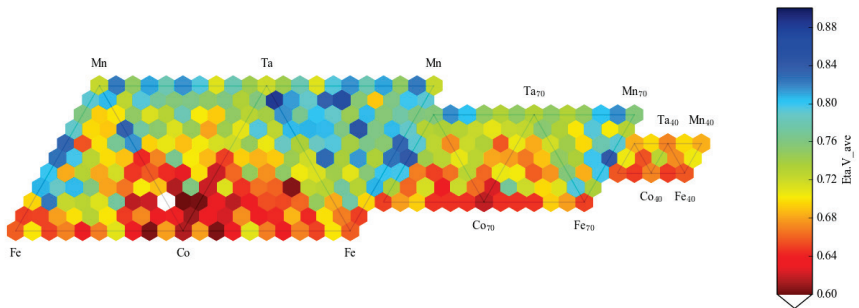
(a) pH 13



(b) pH 9



(c) pH 7



(d) pH 3

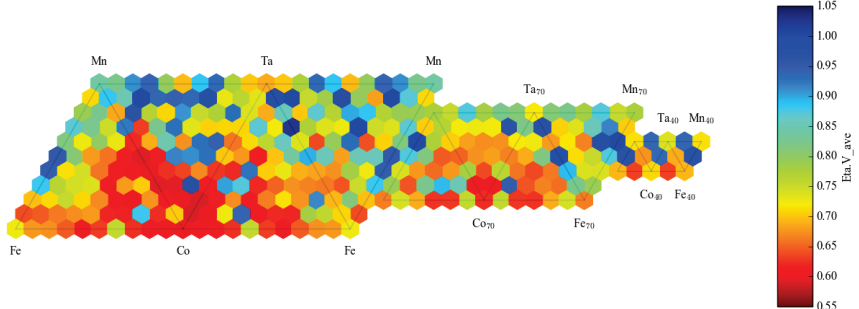
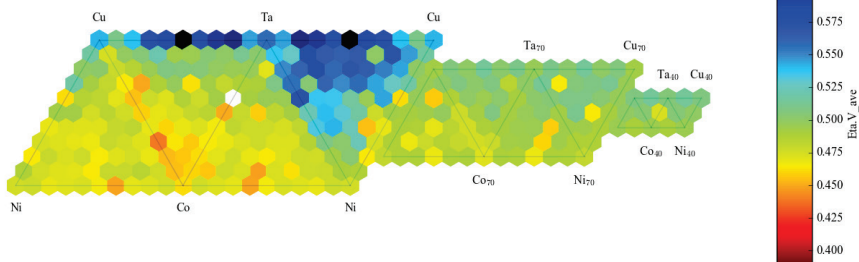
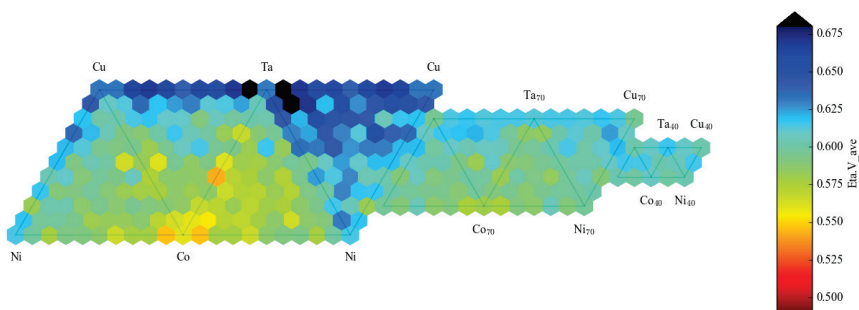


Figure S10-part 2. Composition maps from the (Ni-Fe-Cu-Mn-Co-Ta)O_x composition space: map of η_{OER} at 10 mA cm⁻² for the pseudoquaternary (Fe-Mn-Co-Ta)O_x in (a) pH 13, (b) pH 9, (c) pH 7, (d) pH 3 (note different color scale at each pH).

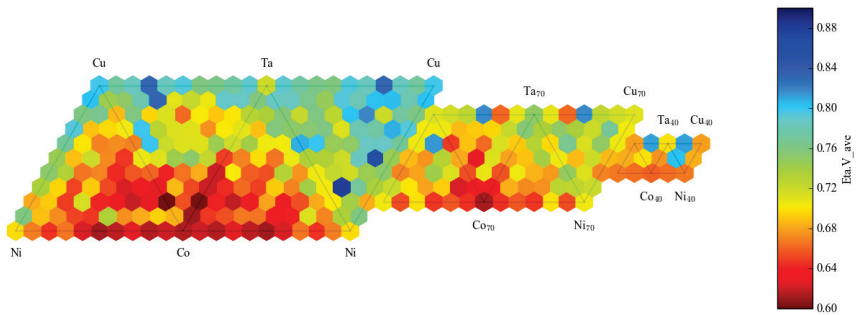
(a) pH 13



(b) pH 9



(c) pH 7



(d) pH 3

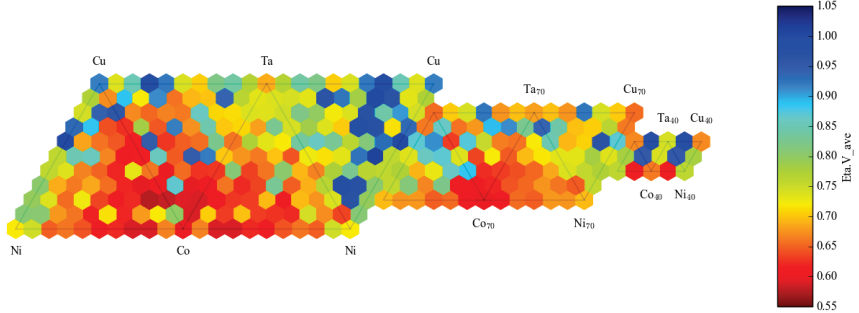
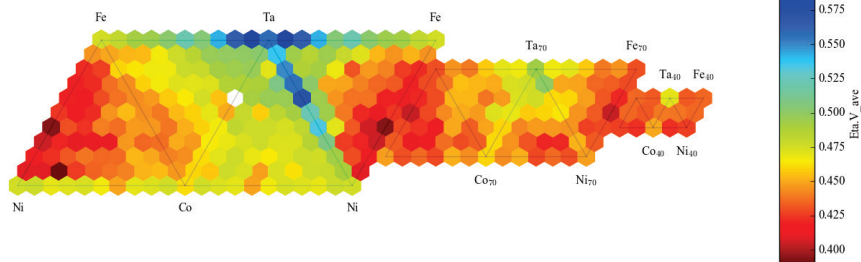
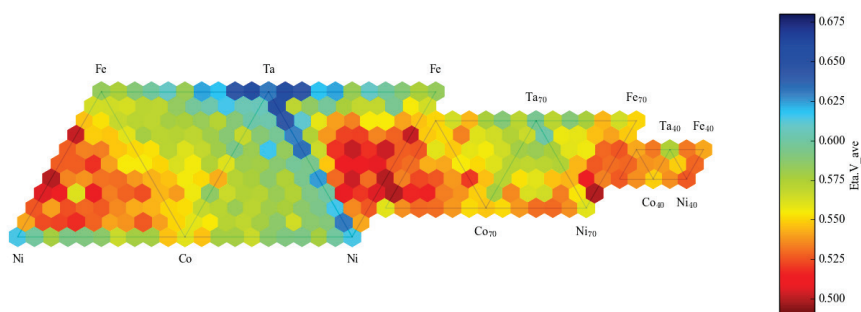


Figure S10-part 3. Composition maps from the (Ni-Fe-Cu-Mn-Co-Ta)O_x composition space: map of η_{OER} at 10 mA cm⁻² for the pseudoquaternary (Ni-Cu-Co-Ta)O_x in (a) pH 13, (b) pH 9, (c) pH 7, (d) pH 3 (note different color scale at each pH).

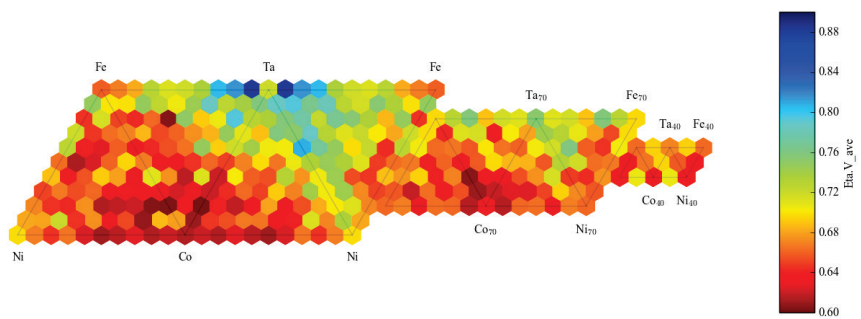
(a) pH 13



(b) pH 9



(c) pH 7



(d) pH 3

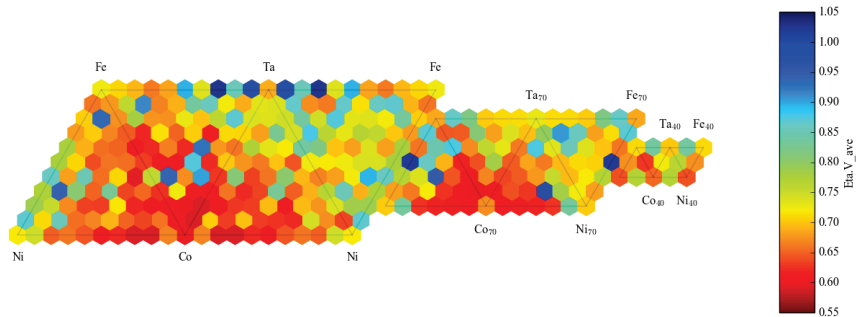
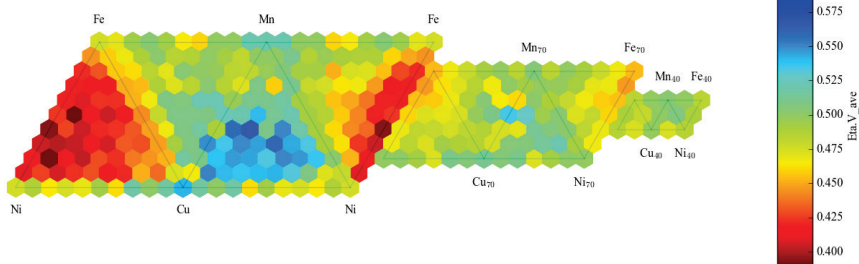
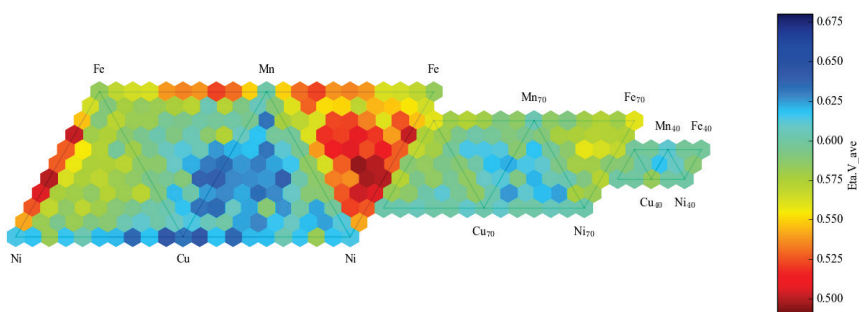


Figure S10-part 4. Composition maps from the (Ni-Fe-Cu-Mn-Co-Ta)O_x composition space: map of η_{OER} at 10 mA cm⁻² for the pseudoquaternary (Ni-Fe-Co-Ta)O_x in (a) pH 13, (b) pH 9, (c) pH 7, (d) pH 3 (note different color scale at each pH).

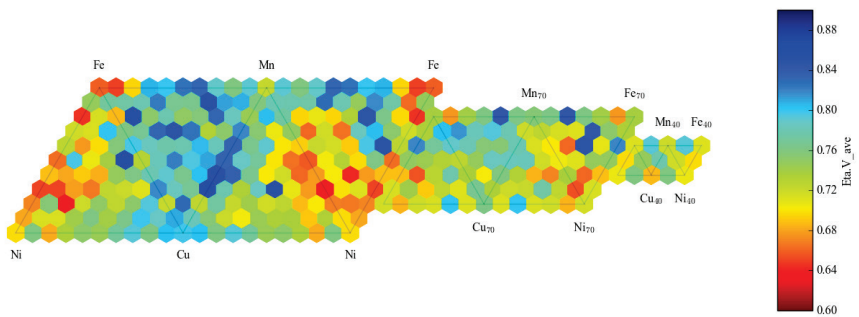
(a) pH 13



(b) pH 9



(c) pH 7



(d) pH 3

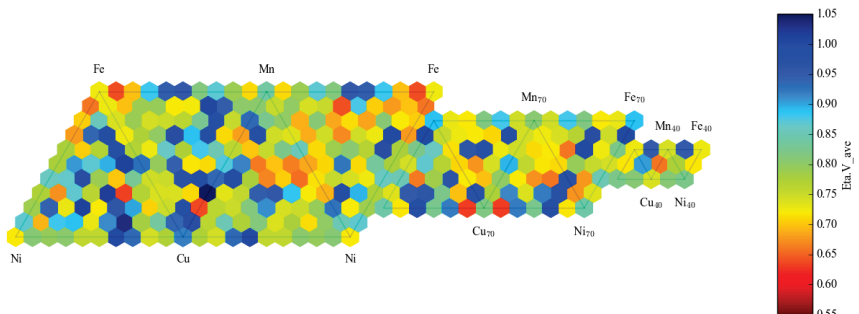
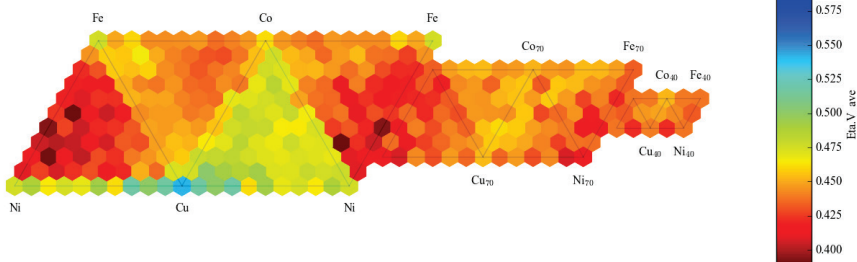
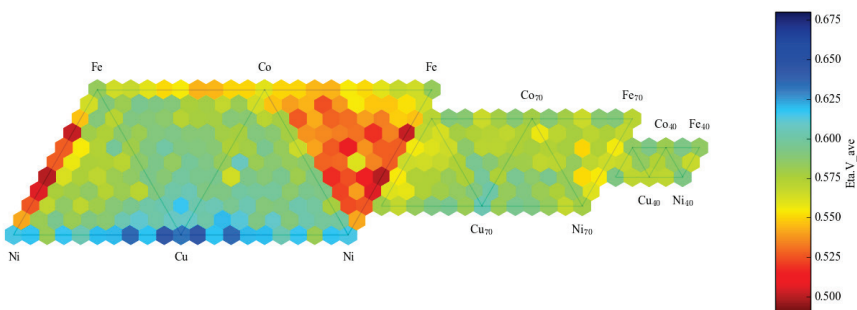


Figure S10-part 5. Composition maps from the (Ni-Fe-Cu-Mn-Co-Ta)O_x composition space: map of η_{OER} at 10 mA cm⁻² for the pseudoquaternary (Ni-Fe-Cu-Mn)O_x in (a) pH 13, (b) pH 9, (c) pH 7, (d) pH 3 (note different color scale at each pH).

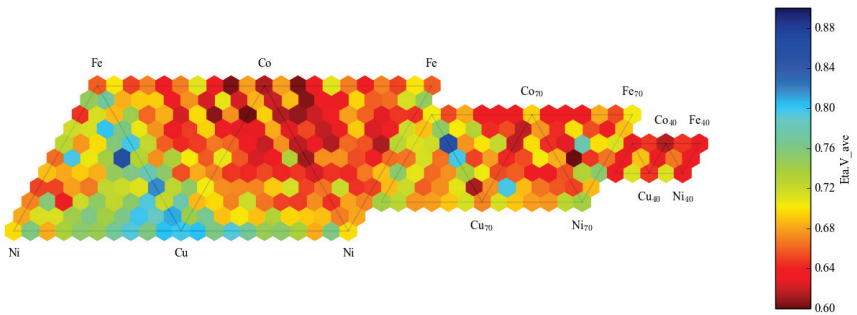
(a) pH 13



(b) pH 9



(c) pH 7



(d) pH 3

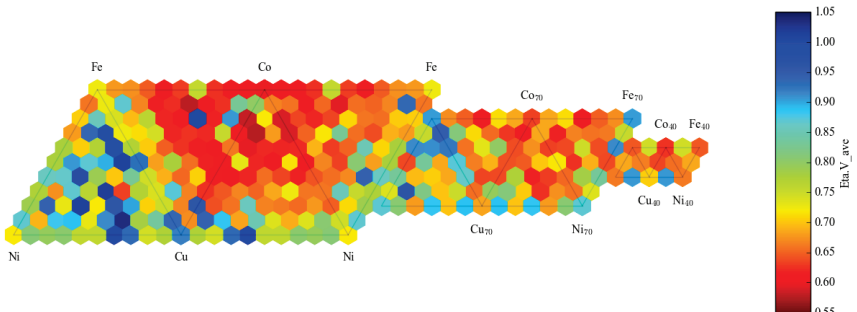
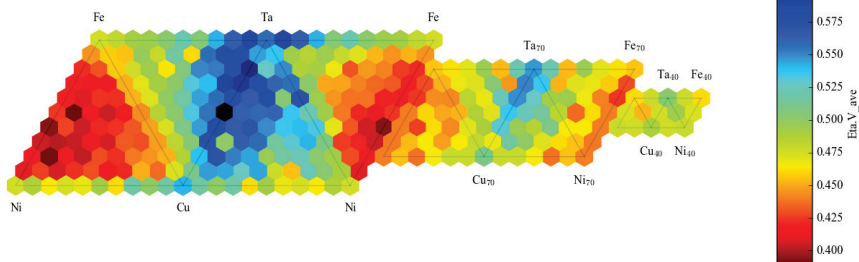
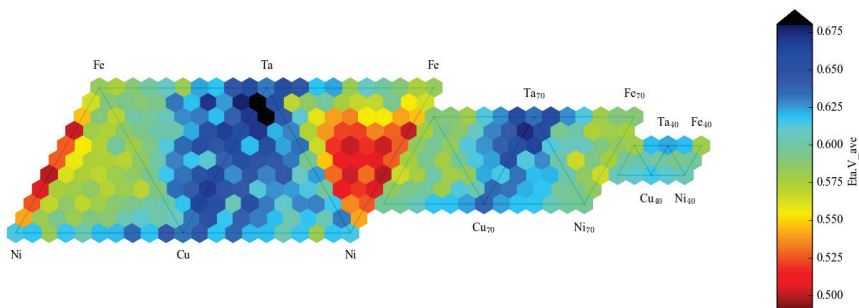


Figure S10-part 6. Composition maps from the (Ni-Fe-Cu-Mn-Co-Ta)O_x composition space: map of η_{OER} at 10 mA cm⁻² for the pseudoquaternary (Ni-Fe-Cu-Co)O_x in (a) pH 13, (b) pH 9, (c) pH 7, (d) pH 3 (note different color scale at each pH).

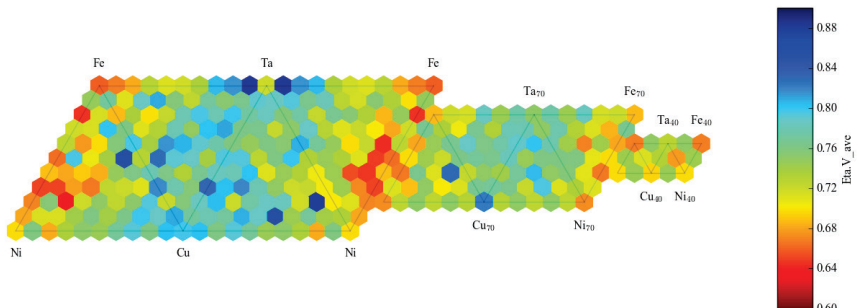
(a) pH 13



(b) pH 9



(c) pH 7



(d) pH 3

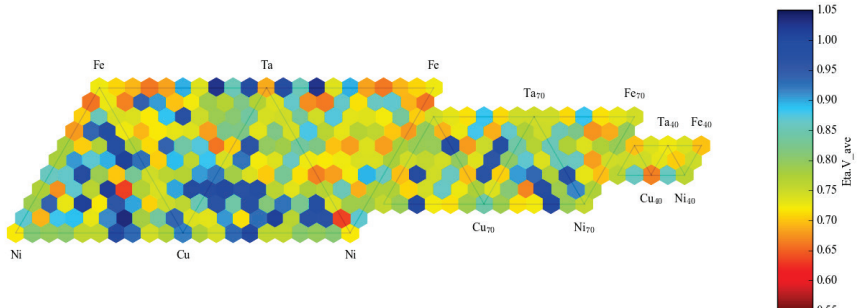
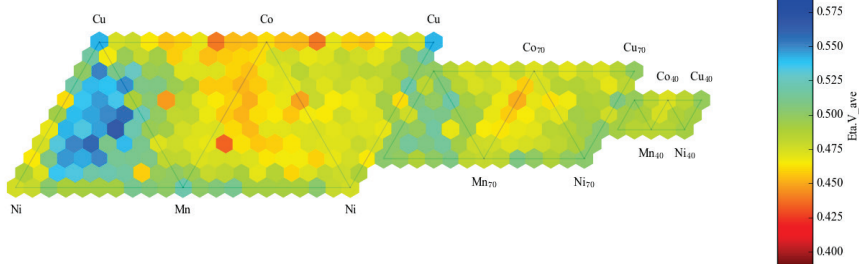
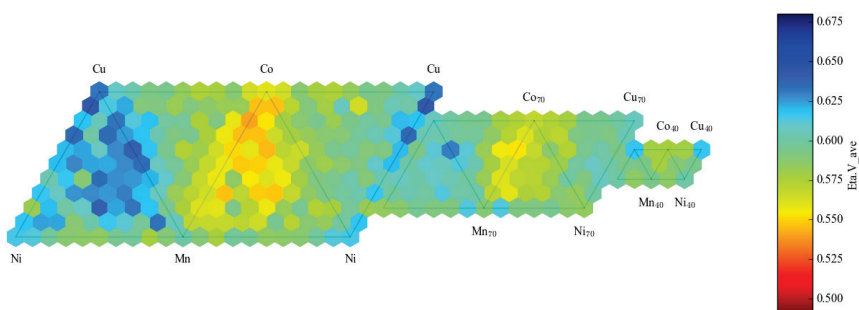


Figure S10-part 7. Composition maps from the (Ni-Fe-Cu-Mn-Co-Ta)O_x composition space: map of η_{OER} at 10 mA cm⁻² for the pseudoquaternary (Ni-Fe-Cu-Ta)O_x in (a) pH 13, (b) pH 9, (c) pH 7, (d) pH 3 (note different color scale at each pH).

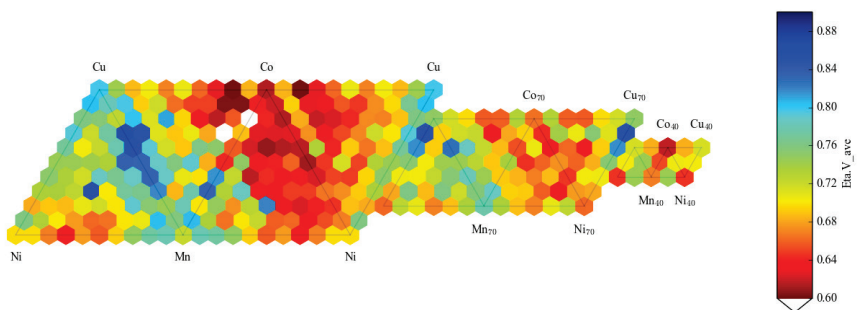
(a) pH 13



(b) pH 9



(c) pH 7



(d) pH 3

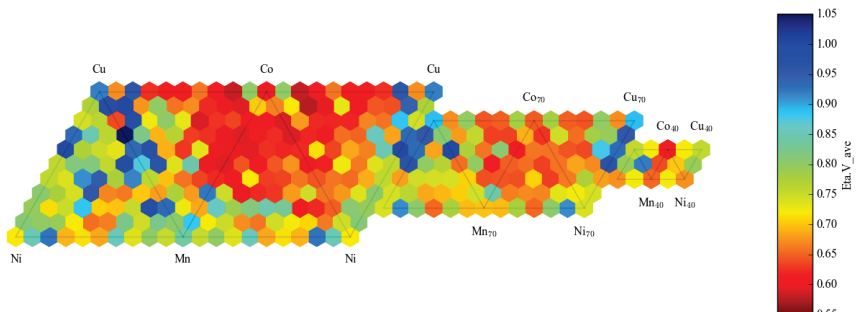
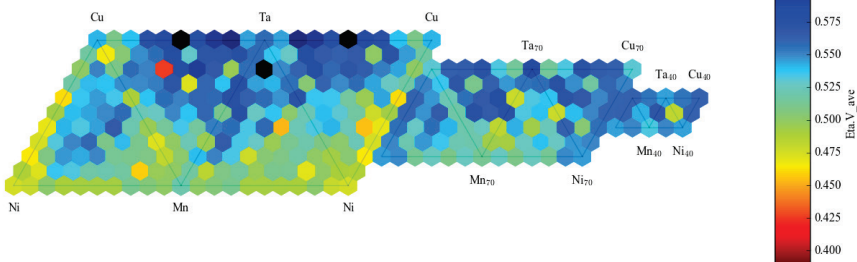
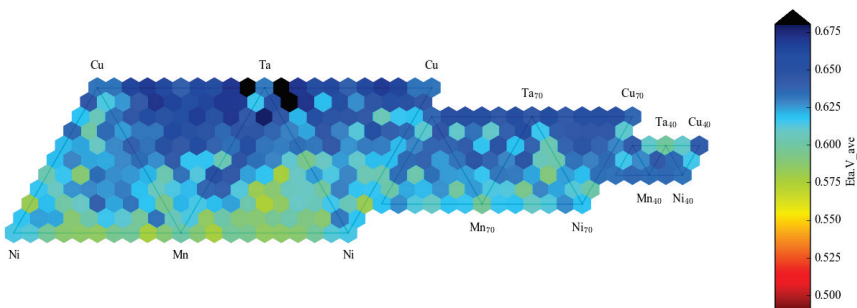


Figure S10-part 8. Composition maps from the (Ni-Fe-Cu-Mn-Co-Ta)O_x composition space: map of η_{OER} at 10 mA cm⁻² for the pseudoquaternary (Ni-Cu-Mn-Co)O_x in (a) pH 13, (b) pH 9, (c) pH 7, (d) pH 3 (note different color scale at each pH).

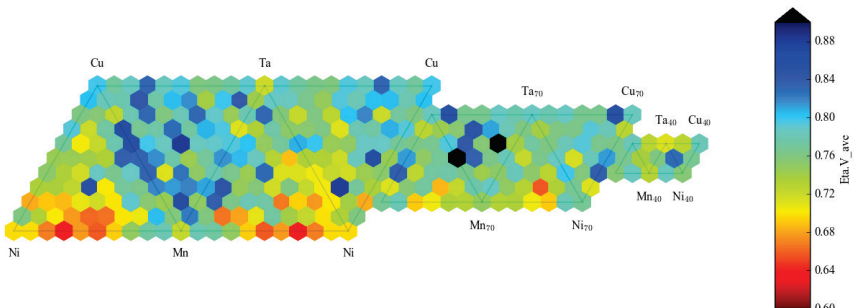
(a) pH 13



(b) pH 9



(c) pH 7



(d) pH 3

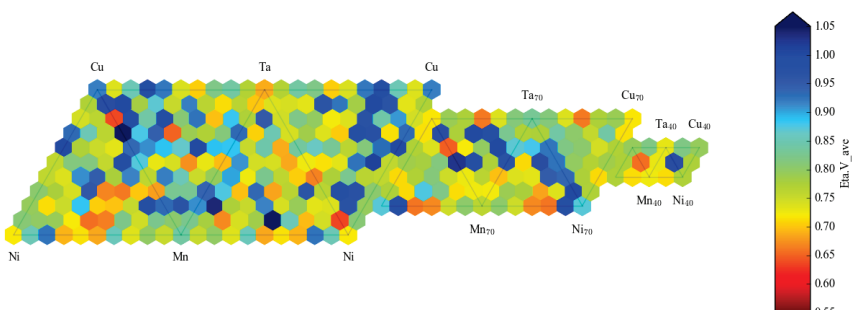
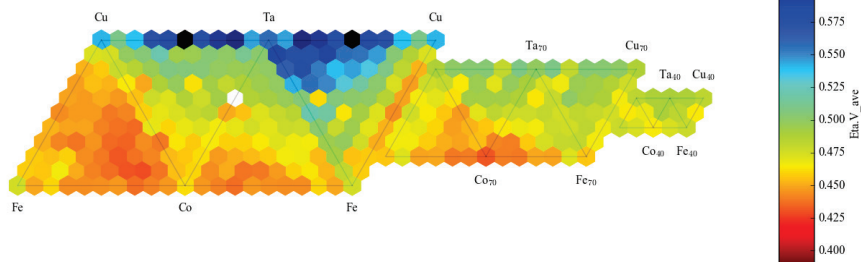
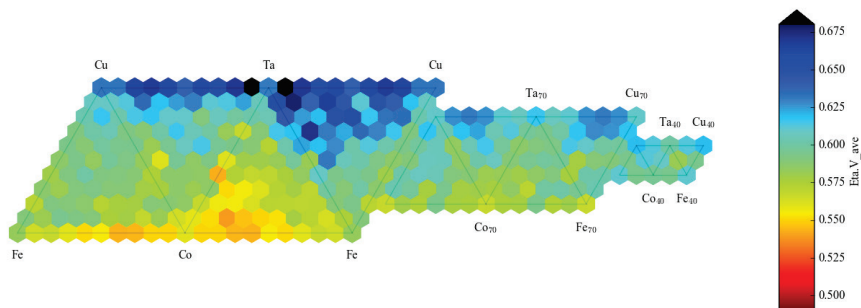


Figure S10-part 9. Composition maps from the (Ni-Fe-Cu-Mn-Co-Ta)O_x composition space: map of η_{OER} at 10 mA cm⁻² for the pseudoquaternary (Ni-Cu-Mn-Ta)O_x in (a) pH 13, (b) pH 9, (c) pH 7, (d) pH 3 (note different color scale at each pH).

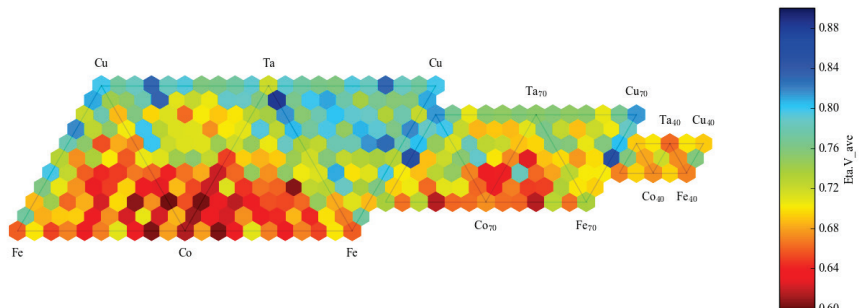
(a) pH 13



(b) pH 9



(c) pH 7



(d) pH 3

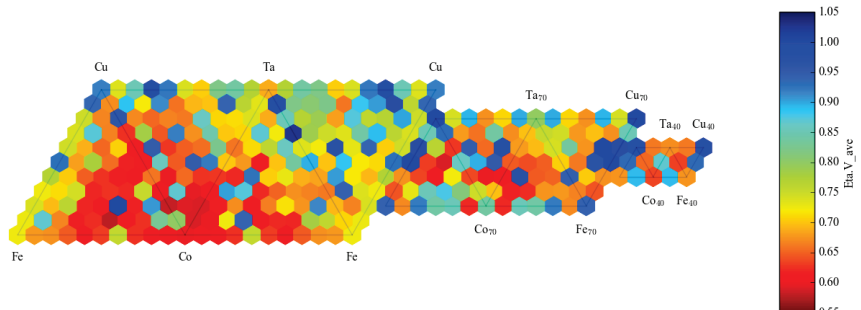
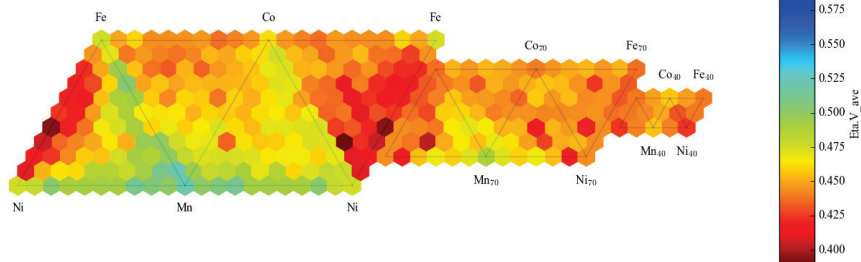
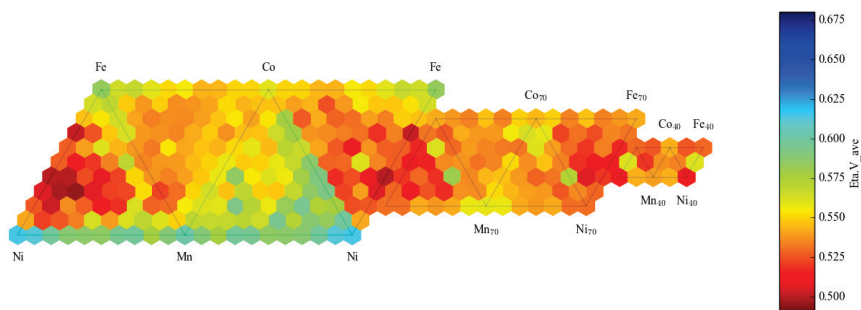


Figure S10-part 10. Composition maps from the (Ni-Fe-Cu-Mn-Co-Ta)O_x composition space: map of η_{OER} at 10 mA cm⁻² for the pseudoquaternary (Fe-Cu-Co-Ta)O_x in (a) pH 13, (b) pH 9, (c) pH 7, (d) pH 3 (note different color scale at each pH).

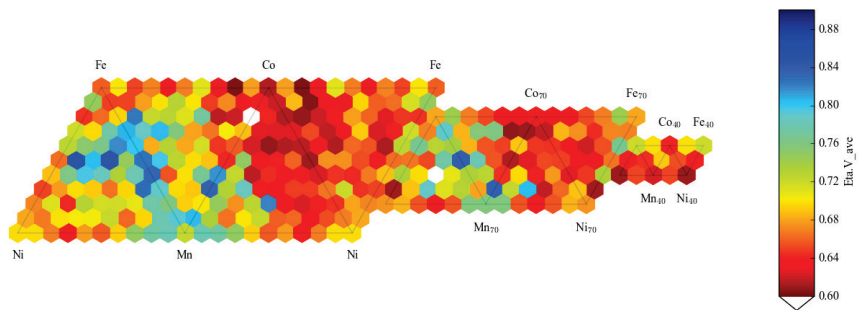
(a) pH 13



(b) pH 9



(c) pH 7



(d) pH 3

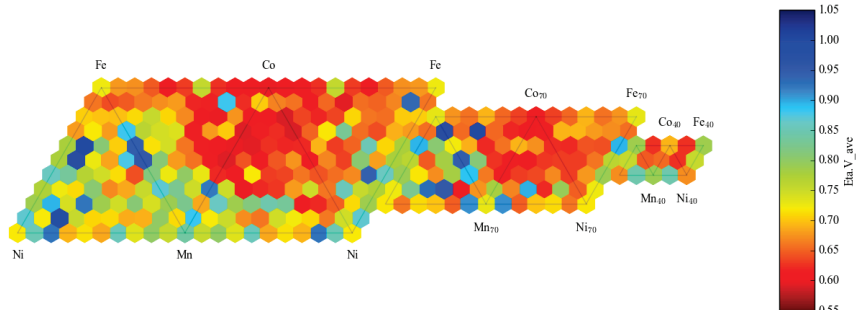
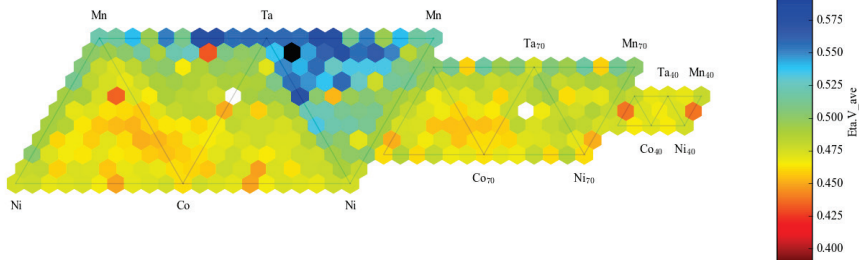
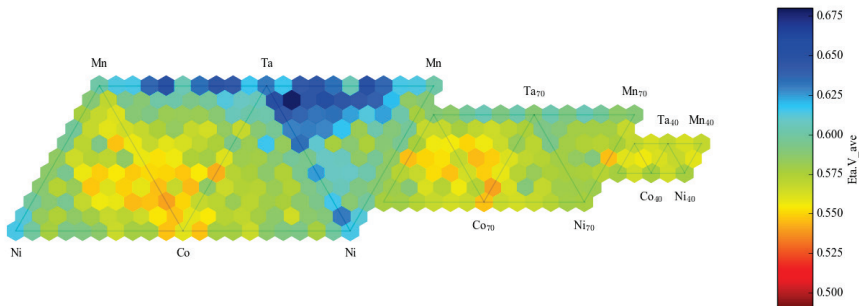


Figure S10-part 11. Composition maps from the (Ni-Fe-Cu-Mn-Co-Ta)O_x composition space: map of η_{OER} at 10 mA cm⁻² for the pseudoquaternary (Ni-Fe-Mn-Co)O_x in (a) pH 13, (b) pH 9, (c) pH 7, (d) pH 3 (note different color scale at each pH).

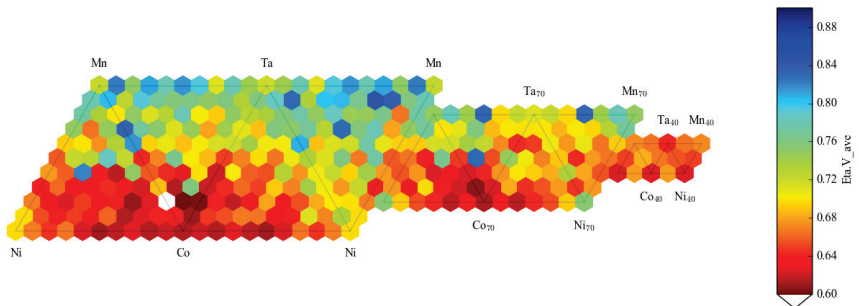
(a) pH 13



(b) pH 9



(c) pH 7



(d) pH 3

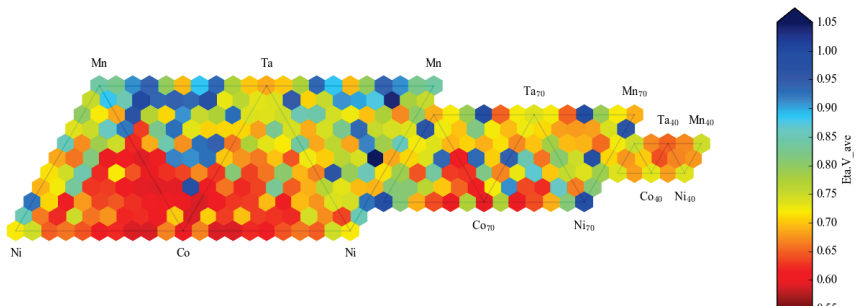
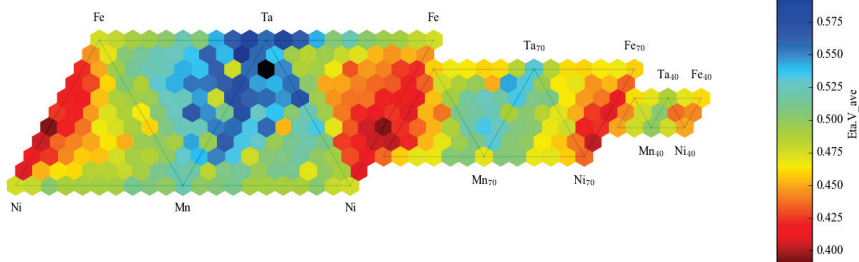
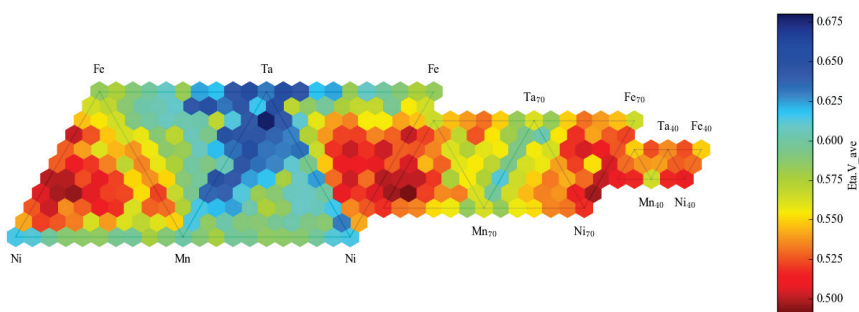


Figure S10-part 12. Composition maps from the (Ni-Fe-Cu-Mn-Co-Ta)O_x composition space: map of η_{OER} at 10 mA cm⁻² for the pseudoquaternary (Ni-Mn-Co-Ta)O_x in (a) pH 13, (b) pH 9, (c) pH 7, (d) pH 3 (note different color scale at each pH).

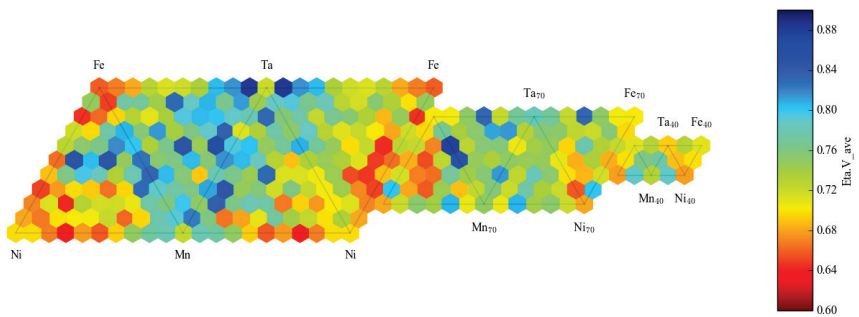
(a) pH 13



(b) pH 9



(c) pH 6.6



(d) pH 3

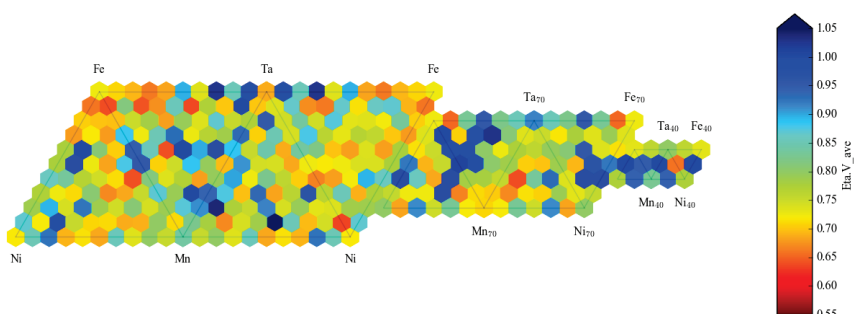
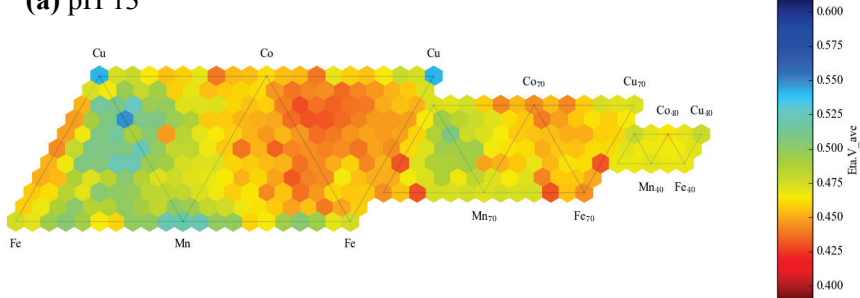
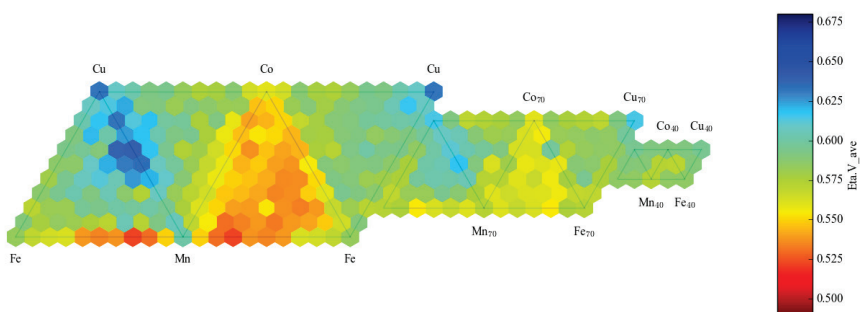


Figure 10-part 13. Composition maps from the (Ni-Fe-Cu-Mn-Co-Ta)O_x composition space: map of η_{OER} at 10 mA cm⁻² for the pseudoquaternary (Ni-Fe-Mn-Ta)O_x in (a) pH 13, (b) pH 9, (c) pH 7, (d) pH 3 (note different color scale at each pH).

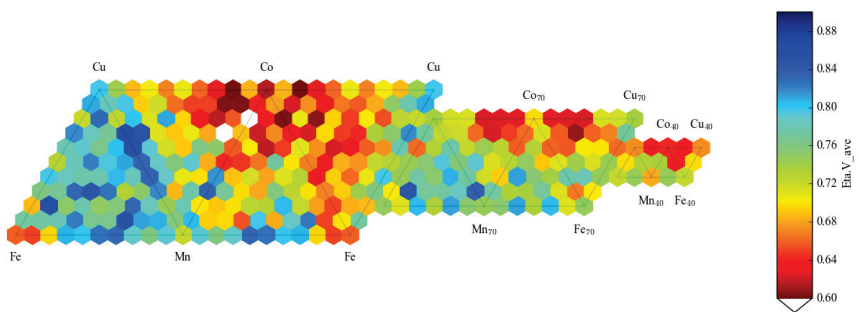
(a) pH 13



(b) pH 9



(c) pH 7



(d) pH 3

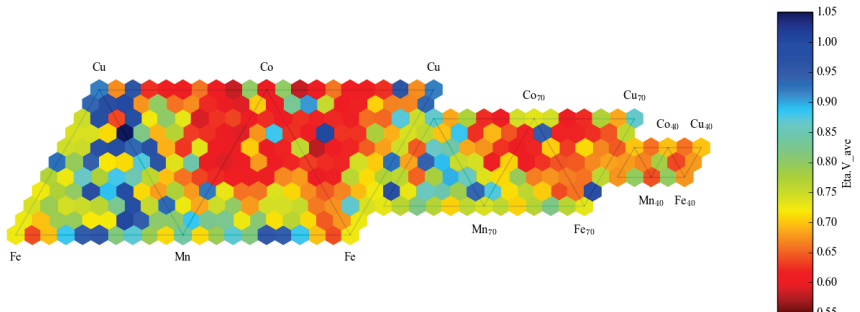
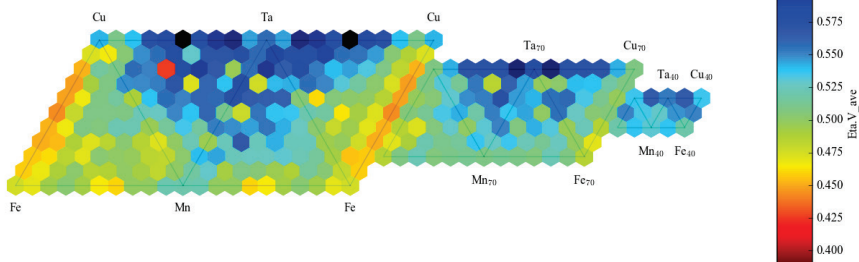
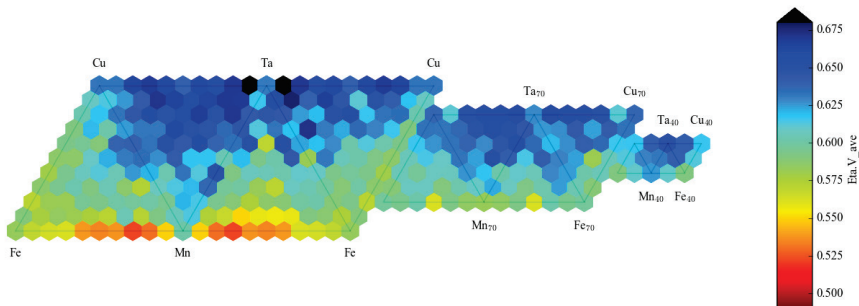


Figure S10-part 14. Composition maps from the (Ni-Fe-Cu-Mn-Co-Ta)O_x composition space: map of η_{OER} at 10 mA cm⁻² for the pseudoquaternary (Fe-Cu-Mn-Co)O_x in (a) pH 13, (b) pH 9, (c) pH 7, (d) pH 3 (note different color scale at each pH).

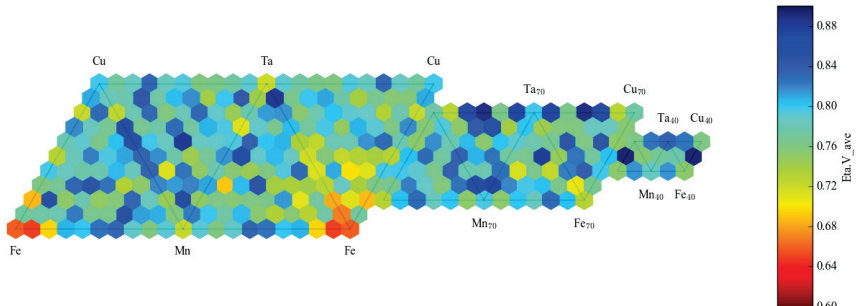
(a) pH 13



(b) pH 9



(c) pH 7



(d) pH 3

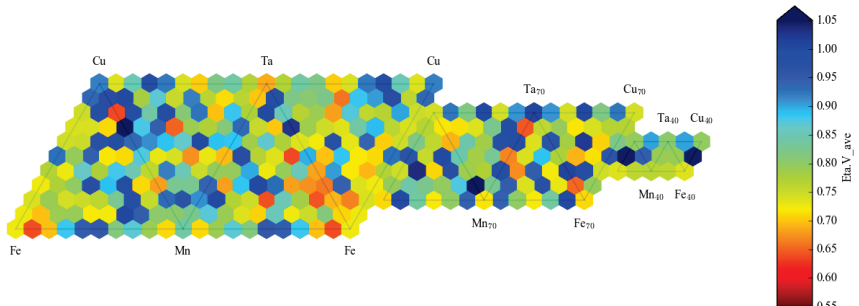


Figure S10-part 15. Composition maps from the (Ni-Fe-Cu-Mn-Co-Ta)O_x composition space: map of η_{OER} at 10 mA cm⁻² for the pseudoquaternary (Fe-Cu-Mn-Ta)O_x in (a) pH 13, (b) pH 9, (c) pH 7, (d) pH 3 (note different color scale at each pH).

References

1. Jones, R. J. R. *et al.* Parallel Electrochemical Treatment System and Application for Identifying Acid-Stable Oxygen Evolution Electrocatalysts. *ACS Combinatorial Science* **17**, 71–75 (2015).
2. Shinde, A. *et al.* High-Throughput Screening for Acid-Stable Oxygen Evolution Electrocatalysts in the (Mn–Co–Ta–Sb)O x Composition Space. *Electrocatalysis* **6**, 229–236 (2014).
3. Gregoire, J. M., Xiang, C., Liu, X., Marcin, M. & Jin, J. Scanning droplet cell for high throughput electrochemical and photoelectrochemical measurements. *Review of Scientific Instruments* **84**, 24102–24107 (2013).